Article

NDST3 deacetylates α-tubulin and suppresses V-ATPase assembly and lysosomal acidification

Qing Tang[1,2] [ID], Mingming Liu[1,2], Yang Liu[1,2], Ran-Der Hwang[1,2], Tao Zhang[1,2] & Jiou Wang[1,2,*] [ID]

Abstract

Lysosomes are key organelles maintaining cellular homeostasis in health and disease. Here, we report the identification of N-deacetylase and N-sulfotransferase 3 (NDST3) as a potent regulator of lysosomal functions through an unbiased genetic screen. NDST3 constitutes a new member of the histone deacetylase (HDAC) family and catalyzes the deacetylation of α-tubulin. Loss of NDST3 promotes assembly of the V-ATPase holoenzyme on the lysosomal membrane and thereby increases the acidification of the organelle. NDST3 is downregulated in tissues and cells from patients carrying the C9orf72 hexanucleotide repeat expansion linked to the neurodegenerative diseases amyotrophic lateral sclerosis (ALS) and frontotemporal dementia (FTD). Deficiency in C9orf72 decreases the level of NDST3, and downregulation of NDST3 exacerbates the proteotoxicity of poly-dipeptides generated from the C9orf72 hexanucleotide repeats. These results demonstrate a previously unknown regulatory mechanism through which microtubule acetylation regulates lysosomal activities and suggest that NDST3 could be targeted to modulate microtubule and lysosomal functions in relevant diseases.

Introduction

The autophagy-lysosomal pathway is a major catabolic process that functions under normal and stressful conditions to enzymatically break down diverse cellular components in membrane compartments. The lysosome is the central organelle in this process (Gatica *et al*, 2018; Yu *et al*, 2018). As the main autophagic process, macroautophagy (hereinafter "autophagy") involves multiple steps, including induction, nucleation of the phagophore, formation of the autophagosome, fusion of the autophagosome with the lysosome,

and autolysosomal degradation (Mizushima *et al*, 2010; Yang & Klionsky, 2010). The dynamic process of autophagy, or the autophagic flux, is critically dependent on normal lysosome activity. As the intracellular degradation center, the lysosome is membrane-bound and contains over 60 different hydrolytic enzymes, including cathepsins (Piao & Amaravadi, 2016; Lawrence & Zoncu, 2019). The lysosomal lumen maintains an acidic environment to optimize hydrolase activities. Given that the cytosolic environment is slightly basic, the lower pH inside the lysosome is actively maintained by the proton-pumping vacuolar-type H^+-ATPase (V-ATPase) located on the lysosomal membrane (Forgac, 2007; Mindell, 2012).

The mammalian V-ATPase is a large protein complex whose activity depends on the assembly of its two multi-subunit domains: a transmembrane V0 domain and a peripheral V1 domain. The V0 domain comprises membrane-embedded subunits a, c, c", d, e, Ac45, and (pro)renin receptor (PRR), responsible for pumping protons across the membrane against the electrochemical gradient (Abbas *et al*, 2020). The V1 domain, consisting of eight subunits (A-H), is an ATP hydrolase located in the cytosol. The free cytosolic V1 domain of V-ATPase is inactive unless it is assembled with the V0 domain. When the V1 domain is associated with the cytosolic side of the V0 domain, it produces energy that V0 uses to pump protons (Maxson & Grinstein, 2014). The assembly of the V-ATPase is a reversible process that is dynamically regulated by metabolic signals such as glucose starvation (Kane, 2000). The C subunit of the V1 domain of V-ATPase can directly interact with microtubules (Tabke *et al*, 2014), and the glucose starvation-induced dissociation of the V1 from the V0 domain is influenced by a microtubule depolymerization agent nocodazole (Noco) (Xu & Forgac, 2001; Tabke *et al*, 2014).

Lysosomal dysfunction can cause aberrant accumulation of its substrates, including misfolded proteins. This accumulation underlies the development of many diseases, including neurodegenerative disorders such as Alzheimer's disease, Parkinson's disease, Huntington's disease, amyotrophic lateral sclerosis (ALS), and frontotemporal dementia (FTD) (Yamamoto & Yue, 2014; Wang *et al*, 2018; Nguyen *et al*, 2019; Nixon, 2020). A hexanucleotide repeat expansion (HRE) in the promoter or intronic region of the *C9orf72* gene is the most common cause of both ALS and FTD (DeJesus-Hernandez *et al*, 2011; Renton *et al*, 2011). The HRE leads to reduced expression of the *C9orf72* gene and potential haploinsufficiency of the encoded protein as an underlying cause of the disease (Haeusler *et*

1   Department of Biochemistry and Molecular Biology, Bloomberg School of Public Health, Johns Hopkins University, Baltimore, MD, USA
2   Department of Neuroscience, School of Medicine, Johns Hopkins University, Baltimore, MD, USA
    *Corresponding author (lead contact). Tel: +1 410 502 0927; Fax: +1 410 955 2926; E-mail: jiouw@jhmi.edu

al, 2014; Waite *et al*, 2014). Although the functions of C9orf72 protein are not fully understood, it has been found in multiple cellular compartments with diverse functions including a physical and functional connection to the lysosomes (O'Rourke *et al*, 2016; Sellier *et al*, 2016; Sivadasan *et al*, 2016; Sullivan *et al*, 2016; Ugolino *et al*, 2016; Yang *et al*, 2016; Ji *et al*, 2020; Wang *et al*, 2020, 2021). The HRE also generates aberrant poly-dipeptides through repeat-associated non-ATG-dependent translation, which have been associated with impaired lysosomal functions in patient cells (Shi *et al*, 2018). Thus, both C9orf72 deficiency and gained proteotoxicity have been implicated in the pathological mechanism of the disease in a lysosome-dependent manner.

In the present study, we have identified N-deacetylase and N-sulfotransferase 3 (NDST3) as a new member of the histone deacetylase (HDAC) family and a potent regulator of lysosomal activity. NDST3 catalyzes the deacetylation of α-tubulin at Lys40; this reduced acetylation, in turn, decreases the assembly of V-ATPase on lysosomes. Thus, loss of NDST3 influences lysosomal acidification and functions. We have also found evidence that the loss of NDST3 exacerbates the proteotoxicity of poly-dipeptides linked to *C9orf72*-ALS/FTD and that NDST3 is downregulated in the cells and tissues of patients affected by this major form of ALS/FTD.

Results

NDST3 is identified as a regulator of bafilomycin toxicity through a CRISPR screen

To further understand the regulation of the autophagy-lysosomal pathway in mammalian cells, we conducted an unbiased CRISPR genetic screen for suppressors of toxicity induced by a well-characterized autophagy inhibitor, bafilomycin A1 (Baf A1). Baf A1 is a macrolide antibiotic that inhibits the function of V-ATPase, thus disrupting the lysosome's ability to acidify and fuse with the autophagosome (Yamamoto *et al*, 1998). The screen was performed in human retinal pigmented epithelial cells (RPE1), which have been shown to have a stable diploid genome amenable to CRISPR editing (Katoh *et al*, 2017). After treatment with Baf A1 at a concentration of 100 nM for 7 days, almost no RPE1 cells survived, confirming their sensitivity to the drug (Appendix Fig S1A). Cells were infected with the lentivirus-expressing sgRNAs from the Human CRISPR Knockout Pooled Library (GeCKOv2) (Sanjana *et al*, 2014). The infected cells were grown under selective conditions with Baf A1 treatment, and surviving cells were isolated for further analysis (Fig 1A). Among the cell colonies that survived the Baf A1 treatment, one of the strongest suppressors was identified to carry a sgRNA targeting NDST3 (Appendix Fig S1B), which we focused on for further analysis.

First, we established the NDST3 knockout (KO) RPE1 cell line and confirmed that the CRISPR-generated mutation was a single-base deletion in exon 5 that resulted in a premature stop codon, thus producing a truncated protein lacking amino acids (aa) 414–873 (Fig 1B and Appendix Fig S2A). NDST3 has three other homologous family members, NDST1, NDST2, and NDST4, among which NDST4 shares 82% homology with NDST3 in its protein sequence (Appendix Fig S2B). Despite the confirmed decrease in mRNA levels expected from the premature stop codon (Appendix Fig S2C), none

of the commercial antibodies that we tested showed specificity for the NDST3 protein in the KO cells. Therefore, we generated and characterized a polyclonal antibody against a region of NDST3 that is relatively unique among its homologs (Fig 1C). The NDST3 polyclonal antibody recognized a strong band by immunoblotting at the molecular size expected for NDST3 in the WT RPE1 cells, but not in the NDST3 KO cells (Fig 1D), demonstrating the specificity of the antibody. The only exception was a minor band in the KO sample that likely resulted from a cross-reacting protein. Indeed, in 2D gel electrophoresis, the signal expected for NDST3 was completely absent from the KO cells when compared to the WT controls (Appendix Fig S2D).

Compared with the WT RPE1 controls, NDST3 KO cells showed much higher cell viability when treated with 25 nM Baf A1 for 72 h (Fig 1E). The observed phenotype could be restored by the exogenous expression of Flag-NDST3 in the KO cells, but not by the Flag-EGFP control at a comparable level (Fig 1F and G). This difference indicates that the highly increased resistance to Baf A1 treatment in NDST3 KO cells was caused by the depletion of the NDST3 protein. To validate these findings in other cell types, we used a shRNA against *NDST3* mRNA to knock down *NDST3* expression in mouse N2a cells and N2a-differentiated neurons and then subjected the cells to the Baf A1 sensitivity assay. The deficiency of NDST3 significantly enhanced the survivability of the cells under Baf A1 treatment (Fig EV1A–F), confirming that the resistance to Baf A1 rendered by the loss of NDST3 is not unique to RPE1 cells.

Loss of NDST3 promotes lysosomal acidification

The cellular toxicity of Baf A1 is primarily attributable to its inhibition of V-ATPase, resulting in an increase in lysosomal pH and impairment of lysosomal function (Yamamoto *et al*, 1998). To understand how the loss of NDST3 renders cells resistant to Baf A1-induced toxicity, we examined the lysosomal acidification in NDST3 KO RPE1 cells versus WT control cells using LysoSensor Yellow/Blue probes. A LysoSensor probe exhibits both pH-dependent dual excitation and dual emission spectral peaks. It has a pK_a of ~4.2 and produces a predominantly yellow fluorescence in acidic organelles but blue fluorescence in less acidic organelles, thus providing a reliable ratiometric measurement of the lysosomal pH independent of probe uptake or other potential variables at a pH range of 3.5–6.0 (Klionsky *et al*, 2016). The LysoSensor Yellow/Blue dextran staining demonstrated that compared with WT cells, NDST3 KO cells exhibited stronger yellow fluorescence but weaker blue fluorescence (Fig 2A). To determine the exact lysosomal pH value, we measured the fluorescence ratio of the LysoSensor probe with a plate reader and determined the pH values against a standard curve obtained by exposing the cells to a series of pH calibration buffers (pH 4.0–6.0) in the presence of monensin and nigericin. The absolute lysosomal pH was found to be 4.8 in the WT cells, consistent with the previous reports (Deriy *et al*, 2009; Dehay *et al*, 2012; Yagi *et al*, 2021), whereas the lysosomal pH was 4.0 in the NDST3 KO cells (Fig 2B and C). Using immunofluorescent staining against LAMP1, we found no change in the number or size of the lysosomes as a result of loss of NDST3 (Fig EV2A). The lysosomal pH measured by the LysoSensor Yellow/Blue dextran was validated by another measurement conducted with LysoSensor Yellow/Blue DND-160, a free cell-permeant LysoSensor dye preferably accumulating in acidic
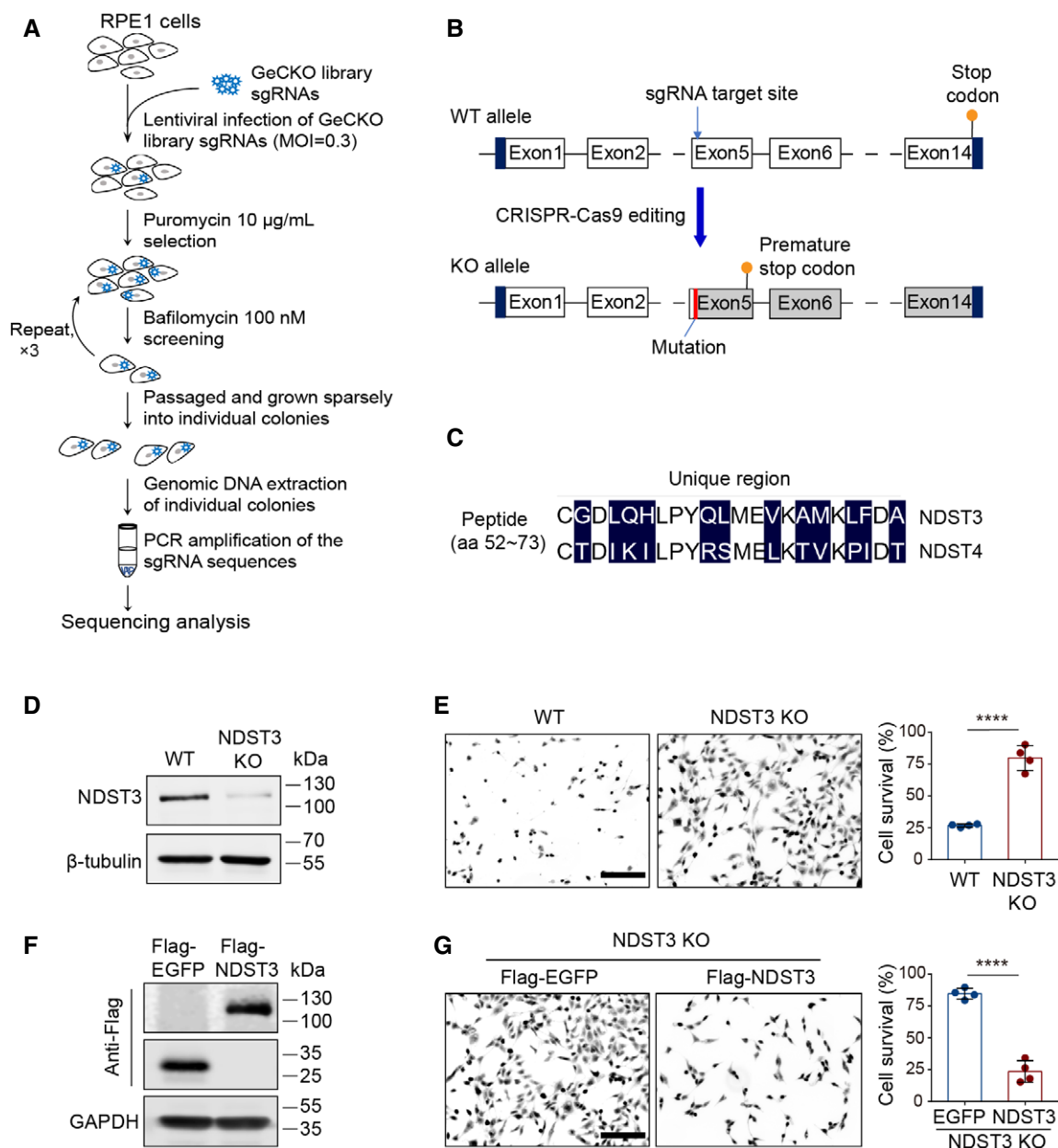
Figure 1. CRISPR/Cas9 knockout library screening shows NDST3 as a regulator of bafilomycin toxicity.

A   A schematic diagram of the CRISPR genetic screen.

B   Generation of a stable NDST3 KO RPE1 cell line.

C   Generation of NDST3 polyclonal antibodies targeting a region of NDST3 unique in the NDST family.

D   Immunoblot analysis of NDST3 in stable NDST3 KO RPE1 cells.

E   Bafilomycin A1 (Baf A1) sensitivity assay for NDST3 KO cells. WT and NDST3 KO RPE1 cell lines were treated with 25 nM Baf A1 for 72 h, and cell survival was measured using calcein AM staining. The cell survival was calculated as the fluorescence intensity (percentage) of the treated cells relative to the untreated cells ($n = 4$ independent cultures, ****$P < 0.0001$).

F   Detection of Flag-NDST3 and Flag-EGFP overexpressed in NDST3 KO cells by immunoblotting with anti-Flag antibodies.

G   Baf A1 sensitivity assay for NDST3 KO cells after the NDST3 restoration. The NDST3 KO cells with stable expression of Flag-NDST3 or Flag-EGFP (control) were treated with 25 nM Baf A1 for 72 h, and cell survival was measured using calcein AM staining. The cell survival was calculated as the fluorescence intensity of the treated cells relative to the untreated cells ($n = 4$ independent cultures, ****$P < 0.0001$).

Data information: Error bars represent ± standard deviation. Scale bar, 200 μm.
Source data are available online for this figure.

organelles such as lysosomes. The LysoSensor Yellow/Blue DND-160 staining also showed much higher acidity in the lysosomes in NDST3 KO cells than those in WT cells against a standard curve (Fig EV2B–D). As a control, a co-staining of the LysoTracker probe and the lysosomal marker LAMP1-GFP stably expressed in live cells showed that nearly all of the acidic vesicles stained with the Lyso-Tracker were LAMP1-GFP-positive lysosomes in both WT and NDST3 KO cells (Fig EV2E). Furthermore, we measured the lysosomal pH values in WT and NDST3 KO cells after the cells were treated with Baf A1. The treatment with Baf A1 (100 nM, 1 h) increased the lysosomal pH in WT and NDST3 KO cells to 5.4 and 4.8, respectively (Fig 2D). Notably, the lysosomal pH remains lower in the NDST3 KO cells than in the WT cells, but the lysosomal pH in the NDST3 KO cells treated with Baf A1 was comparable to that in the WT cells without the Baf A1 treatment. These results demonstrated that loss of NDST3 promotes acidification of lysosomes and thereby neutralizes the Baf A1-induced basification of the lysosomes.

Although hydrolytic enzymes resident in the lysosome need an acidic environment to be activated, over-acidification may suppress their activation (Soyombo *et al*, 2006; Kiselyov & Muallem, 2008; Venkatachalam *et al*, 2008). Cathepsin B (Cat B) is a cysteine protease involved in lysosomal proteolysis and implicated in the pathogenesis of neurodegenerative diseases (Gan *et al*, 2004; Stoka *et al*, 2016). Consistent with a previous report that over-acidification of the lysosome suppresses the proteolytic activity of cathepsins (Mach *et al*, 1994), we observed that the maturation of Cat B from the inactive precursor proCat B to the lower-molecular-weight mature form was impaired in an *in vitro* maturation assay using purified Cat B proteins, when the pH was below 4.5 (Fig EV3A). Interestingly, we observed that the ratio of mature Cat B to its precursor in the isolated lysosomes was significantly lower in NDST3 KO cells than in WT cells (Fig 2E). Accordingly, when the Cat B proteolytic activity was measured using the Magic Red Cat B assay, which is based on an engineered Cat B substrate that generates red fluorescence upon cleavage and validated using a Cat B inhibitor (Appendix Fig S3) (Mauvezin *et al*, 2015), NDST3 KO cells showed reduced Cat B activity when compared with WT cells (Fig 2F). Furthermore, the neutralization of lysosomal acidification with Baf A1 (100 nM, 1 h) resulted in diminished Magic Red fluorescence in WT cells but enhanced the signals in NDST3 KO cells (Fig 2F). As a control, there was no change observed in the colocalization of Cat B with the lysosomal marker LAMP1 in NDST3 KO cells (Fig EV3B), suggesting that the impaired Cat B maturation does not result from any trafficking defects but take place in the lysosomes.

To measure the lysosomal degradative activity, we used a pH-insensitive Alexa Fluor 488-dextran probe, which can be taken up by the cells through endocytosis and degraded in the lysosomes (Liu *et al*, 2018). Through a chase experiment to examine the degradation of the Alexa Fluor 488-dextran probe, we observed a significant impairment of the lysosomal activity in NDST3 KO cells. Under normal conditions, a large portion of the fluorescent probe was degraded in the WT cells after a 4-h chase; however, the degradation was significantly slower in the NDST3 KO cells (Fig 2G). With the treatment of Baf A1 (100 nM, 1h), the degradation of the probe

Figure 2. Loss of NDST3 promotes lysosomal acidification and modulates lysosomal function.

A   Determination of lysosomal pH with the ratiometric probe LysoSensor Yellow/Blue dextran. WT and NDST3 KO RPE1 cells were stained with LysoSensor Yellow/Blue dextran and then observed for fluorescence. Yellow fluorescence represents more acidic lysosomal environment, and blue fluorescence represents more neutral lysosomal environment.

B   The calibration curve for the lysosome pH. RPE1 cells were incubated with a series of pH calibration buffers (pH 4.0, 4.5, 5.0, 5.5, and 6.0) in the presence of 10 μM monensin and 30 μM nigericin and examined for the fluorescence ratio of LysoSensor Yellow/Blue dextran staining by a plate reader.

C   Lysosomal pH values in WT and NDST3 KO RPE1 cells calculated from the fluorescence ratio of LysoSensor Yellow/Blue dextran staining against the pH calibration curve in (B) ($n = 3$ independent cultures, *$P = 0.0242$).

D   Lysosomal pH values measured for WT and NDST3 KO RPE1 cells after the treatment with Baf A1 (100 nM, 1 h) ($n = 3$ independent cultures, *$P = 0.0305$).

E   SDS–PAGE and immunoblotting analysis of the maturation of Cathepsin B (Cat B) in the lysosomes isolated from WT and NDST3 KO RPE1 cells. The ratio of mature Cat B (heavy chain) to pro-cathepsin B (ProCat B) was calculated to evaluate the maturation of Cat B ($n = 3$ independent experiments, ***$P = 0.0007$). LAMP1 was set as a loading control.

F   Magic Red assay for Cat B proteolytic activity. WT and NDST3 KO RPE1 cells were treated with vehicle (VEH) or Baf A1 (100 nM, 1 h) and then stained with MR-(RR)$_2$ to measure the Cathepsin B activity ($n = 48$ cells in the VEH-treated WT group, $n = 37$ cells in the VEH-treated NDST3 KO group, $n = 64$ cells in the Baf A1-treated WT group, $n = 42$ cells in the Baf A1-treated NDST3 KO group, ****$P < 0.0001$).

G   Alexa Fluor (AF) 488-dextran degradation assay. WT and NDST3 KO RPE1 cells were loaded with AF488-dextran in culture medium and observed for fluorescence. The AF488 fluorescence signals without a chase period, with a 4-h chase period, and with the 4-h chase period in the presence of Baf A1 (100 nM, 1 h) were recorded as fluorescence of uptake, chase, and chase with Baf A1, respectively. The AF488 intensity per cell was quantified and calculated into degradation percentage according to the equation in *Materials and Methods* ($n = 62$ cells in the VEH-treated WT group, $n = 36$ cells in the VEH-treated NDST3 KO group, $n = 65$ cells in the Baf A1-treated WT group, $n = 78$ cells in the Baf A1-treated NDST3 KO group, ****$P < 0.0001$).

H   Analysis of the conversion of LC3B-I to LC3B-II and the levels of p62. WT and NDST3 KO RPE1 cells were cultured with or without 100 nM rapamycin (Rapa) for 6 h and LC3B-I, LC3B-II, p62, and GAPDH levels in the total cell lysates were determined by SDS–PAGE and immunoblotting. The ratios of LC3B-II to LC3B-I ($n = 3$ independent experiments, *$P = 0.0451$, **$P = 0.0042$) and the p62 levels normalized to β-tubulin ($n = 3$ independent experiments, *$P(Rapa^-) = 0.0158$, *$P(Rapa^+) = 0.0183$) are quantified.

I   The LC3 turnover assay. WT and NDST3 KO RPE1 cells were cultured in the presence of 100 nM Rapa and with or without 50 μM chloroquine (CQ) for 6 h, and LC3B-II levels in the total cell lysates were determined by immunoblotting. The fold change of LC3B-II levels was shown by comparing the samples with and without CQ treatment ($n = 6$ independent experiments, ***$P = 0.0007$).

J   The LC3 turnover assay after a 48-h Baf A1 treatment. WT and NDST3 KO RPE1 cells were cultured with 25 nM Baf A1 for 48 h and analyzed for the LC3B-II fold change as in (I) ($n = 6$ independent experiments, **$P = 0.0014$).

Data information: Error bars represent ± standard deviation. Scale bar, 10 μm.
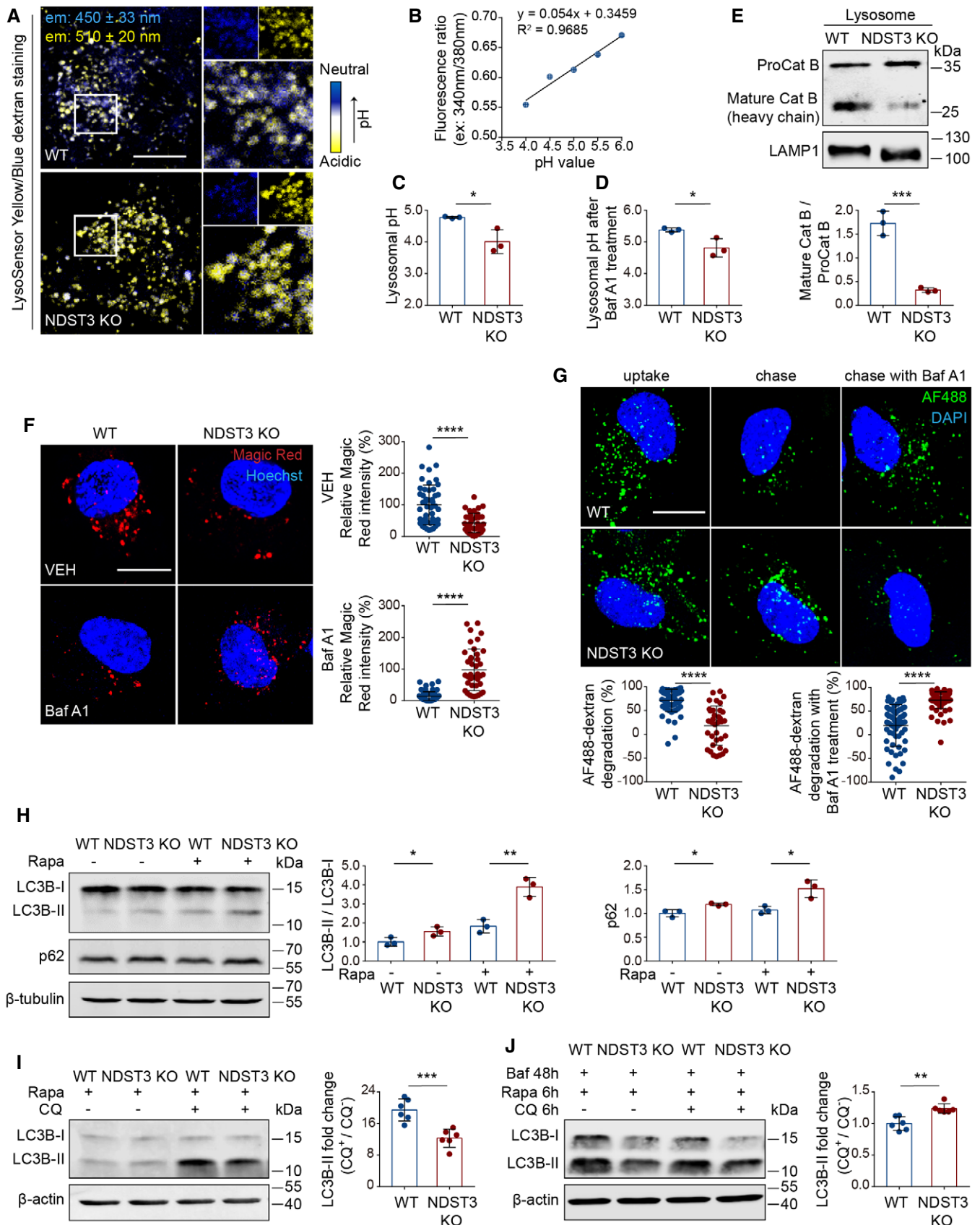Source data are available online for this figure.

Figure 2.

was significantly decreased in WT cells. In contrast, the degradation of the probe in the NDST3 KO cells was significantly accelerated by the treatment with Baf A1 (Fig 2G). These results support the notion that the lysosomal activity is reduced as a result of its hyperacidification upon loss of NDST3, a deficit that can be alleviated by the Baf A1 treatment.

Next, we asked if the lysosomal dysfunction in NDST3 KO cells has any impact on autophagic activities. The autophagy marker LC3B-I is converted to the lipidated form LC3B-II, which is recruited to the autophagosomal membrane and degraded in the lysosome after the fusion of the two organelles. We observed that the ratio of LC3B-II to LC3B-I was increased when cells were depleted of NDST3 under basal autophagy conditions (Fig 2H). Treatment with rapamycin, an mTOR inhibitor that induces autophagy, led to a more significant increase in the LC3B-II/LC3B-I ratio in NDST3 KO cells than in WT controls (Fig 2H). The accumulation of LC3B-II relative to LC3B-I indicates that the autophagy-lysosomal pathway is perturbed by the loss of NDST3. Moreover, p62, another substrate in the autophagy-lysosomal pathway, was significantly increased in NDST3 KO cells compared to WT controls under both basal and rapamycin-induced autophagy conditions (Fig 2H). The accumulation of LC3B-II and p62 suggests that the degradation of autophagosomes by the lysosome may be impaired upon loss of NDST3. To assess the changes in the autophagic flux as a consequence of the loss of NDST3, we performed the LC3B-II turnover assay by treating WT and NDST3 KO cells with the lysosomal inhibitor chloroquine, which blocks the fusion of autophagosomes with lysosomes (Mauthe *et al*, 2018). The chloroquine-induced accumulation of LC3B-II was significantly lower in NDST3 KO cells than in the WT controls (Fig 2I), indicating that the autophagic flux was slowed in the absence of NDST3. Furthermore, under a prolonged treatment with Baf A1 (25 nM, 48 h), although the autophagic flux as measured by the LC3B-II turnover was completely blocked in WT cells, the NDST3 KO cells were able to maintain a partial autophagic flux (Fig 2J), consistent with the compensatory effect of lysosomal acidification upon loss of NDST3 that renders cells resistant to Baf A1-induced toxicity.

During the Western blotting analysis of LAMP1, we noticed that LAMP1 from NDST3 KO cells migrated slightly faster on SDS–PAGE than that from WT cells (Fig 2E). Treatment with swainsonine (SWN), an inhibitor of protein glycosylation, resulted in the same shift in the migration of LAMP1 from WT cells while not affecting LAMP1 from NDST3 KO cells (Appendix Fig S4A), suggesting the migration shift was a consequence of deglycosylation of LAMP1. The SWN treatment alone did not cause lysosomal hyperacidification or dysfunction (Appendix Fig S4B and C), as observed in NDST3 KO cells, indicating that the deglycosylation of LAMP1 was not responsible for the changes in lysosomal pH and functions in the NDST3 KO cells.

Loss of NDST3 increases the V-ATPase V1-V0 holoenzyme on lysosomal membranes

Lysosomal acidification is primarily regulated by the V-ATPase complex, which is responsible for the proton transitions between the cytosol and the lysosomal lumen (Breton & Brown, 2013; Chung *et al*, 2019). The V1 peripheral domain and the V0 integral membrane domain of the V-ATPase complex are each composed of
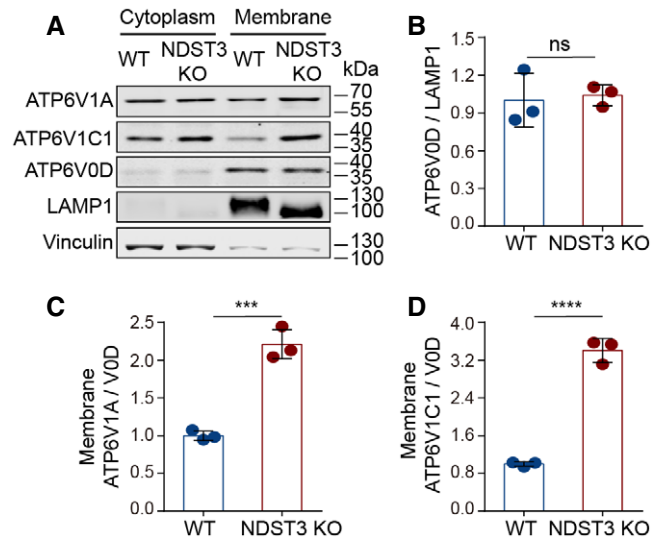

Figure 3. Loss of NDST3 promotes the assembly of the V-ATPase V1-V0 holoenzyme.

A   To examine the levels of the V-ATPase V1-V0 holoenzyme in WT and NDST3 KO RPE1 cells, cytosolic and membrane fractions were analyzed by immunoblotting using antibodies against the V-ATPase subunits V1A (ATP6V1A), V1C1 (ATP6V1C1), and V0D (ATP6V0D). LAMP1 and vinculin were used as loading controls for membrane proteins and cytosolic proteins, respectively.

B   Quantification of the levels of ATP6V0D relative to LAMP1 in the membrane fraction from (A) ($n = 3$ independent experiments, $P = 0.7786$).

C, D   Ratios of ATP6V1A (C) and ATP6V1C1 (D) to ATP6V0D in the membrane fraction from (A) to represent the assembly of the V-ATPase V1-V0 holoenzyme ($n = 3$ independent experiments, ***$P = 0.0005$, ****$P < 0.0001$).

Data information: Error bars represent ± standard deviation.
Source data are available online for this figure.

multiple subunits. The cytosolic V1 subunits need to associate with the membrane-embedded V0 subunits to form the V1-V0 holoenzyme in order to form a functional proton pump (Seol *et al*, 2001; Abbas *et al*, 2020) (Appendix Fig S5). To understand how the loss of NDST3 increases lysosomal acidification, we examined the levels of the V-ATPase V1-V0 holoenzyme assembled on the lysosome membrane in WT and NDST3 KO cells. We isolated the membrane fraction of cells and quantified the abundance of membrane-associated V1 subunits V1A and V1C1 relative to the V0 subunit V0D as an indicator of assembled V1-V0 holoenzymes. The relative levels of V0D in the membrane fractions were comparable in WT and NDST3 KO cells after normalization against the lysosomal marker LAMP1 (Fig 3A and B), suggesting that the density of the V-ATPase V0 domain on the lysosomes was not altered in the mutant cells. However, the levels of the V1 domain docked onto the V0 domain, as measured by the levels of V1A and V1C1 in the membrane fraction, were significantly increased in NDST3 KO cells when compared to those in WT cells (Fig 3A, C and D), indicating an increase of V-ATPase V1-V0 holoenzymes in the absence of NDST3. These data suggest that loss of NDST3 increases lysosomal acidification by promoting the assembly of the V-ATPase holoenzyme.

NDST3 regulates assembly of V-ATPase holoenzyme via microtubule acetylation

We investigated how loss of NDST3 promotes the assembly of V-ATPase holoenzyme on the lysosome. A change in the level of a specific subunit such as ATP6V1C1 does not appear to be the cause for the increase of V-ATPase holoenzymes, since overexpression of ATP6V1C1 in WT cells did not change the level of membrane-bound ATP6V1C1 or the level of another subunit ATP6V1A in any fraction (Appendix Fig S6A–E), suggesting an alternative mechanism related to the assembly of V-ATPase subunits. It was reported that microtubule stability affects V-ATPase disassociation (Xu & Forgac, 2001). Additionally, lysosomal positioning and movement are dependent on microtubules (Matteoni & Kreis, 1987). To test whether the microtubule is required for the recruitment of V-ATPase V1 subunits to the lysosome, we treated RPE1 cells with the microtubule depolymerization agent Noco or a stabilizing agent Taxol and observed significantly decreased or increased colocalization of ATP6V1C1 with the lysosomes marked by LAMP1-GFP, respectively (Fig EV4A and B), suggesting that the microtubule stability is critical for the recruitment of V1 subunits to the lysosome.

Microtubule acetylation is a hallmark of stable microtubules, and specifically, the acetylation of α-tubulin at Lys40 protects the microtubules from depolymerization (Janke & Montagnac, 2017; Xu *et al*, 2017). Through an immunostaining assay against LAMP1-GFP, ATP6V1C1, and α-tubulin acetylated at Lys40 in RPE1 cells, we found that LAMP1-GFP and ATP6V1C1 colocalized in a perinuclear area where acetylated microtubules are relatively enriched and that treatment of Noco disrupted the colocalization of LAMP1-GFP and ATP6V1C1 in the perinuclear area (Fig 4A and B). To test whether microtubule acetylation plays a crucial role in the assembly of the V-ATPase holoenzyme, we treated RPE1 cells with tubacin, a

selective inhibitor of HDAC6 as one of the known α-tubulin deacetylases, to elevate the acetylation level of α-tubulin in the cells (Fig 4 G). Then, we fractionated the cells and examined the levels of the V-ATPase V1-V0 holoenzyme in the membrane fractions. The level of the integral domain subunit V0D in the membrane fraction was unchanged under the treatment of tubacin (Fig 4C and D); however, the relative amounts of the peripheral domain subunits V1A and V1C1 assembled onto V0D were increased in tubacin-treated cells when compared to those in VEH-treated cells (Fig 4C, E and F), suggesting that the microtubule acetylation increased the assembly of the V-ATPase holoenzyme. Moreover, treatment with the microtubule depolymerizing agent Noco, which also substantially reduced the level of microtubule acetylation (Fig 4G), completely ablated the effect of tubacin on the V-ATPase holoenzyme assembly (Fig 4C–F). Furthermore, when we overexpressed the deacetylase HDAC6 to downregulate the level of acetylated α-tubulin (Fig 4L), the level of V0D in the membrane fraction was not altered (Fig 4H and I), but the levels of V1A and V1C1 assembled onto ATP6V0D were substantially decreased as a result of HDAC6 expression (Fig 4H, J and K), confirming that microtubule acetylation plays a critical role in mediating the V-ATPase holoenzyme assembly.

In accordance with the increase of V-ATPase holoenzymes upon loss of NDST3, we observed higher levels of microtubule acetylation (Fig 4M and N) and increased colocalization of the lysosomes and V-ATPase V1 subunits (Fig 4M and O) in NDST3 KO cells compared to those in WT cells. Furthermore, when HDAC6 was overexpressed in the NDST3 KO cells to downregulate the acetylation of α-tubulin, we found that the levels of ATP6V1A and ATP6V1C1 assembled onto ATP6V0D were significantly decreased (Fig 4P–T), confirming that the increase in the assembly of the V-ATPase V1-V0 holoenzyme induced by loss of NDST3 was dependent on the microtubule acetylation.

Figure 4. The assembly of the V-ATPase V1-V0 holoenzyme is dependent on microtubule acetylation.

A, B Perinuclear enrichment and colocalization of acetylated microtubules, lysosomes, and V-ATPase V1 subunits. RPE1 cells stably expressing LAMP1-GFP were treated with vehicle (VEH) or 10 μg/ml nocodazole (Noco) for 6 h before being fixed and subjected to immunofluorescence staining with antibodies against ATP6V1C1 and acetylated-α-tubulin (Ac-α-tubulin). The nucleus was stained with DAPI. Representative images of LAMP1-GFP, ATP6V1C1, and Ac-α-tubulin immunostaining are shown in (A). Representative distribution profiles of Ac-α-tubulin, LAMP1-GFP and ATP6V1C1 were plotted by Fiji software in (B).

C–F The assembly of V-ATPase V1-V0 holoenzymes after treatment with an α-tubulin deacetylase inhibitor or a microtubule depolymerizing agent. RPE1 cells were treated with VEH, tubacin (2.5 μM, 20 h), Noco (10 μg/ml, 6 h), or in combination. Cytosolic and membrane fractions were then extracted and analyzed by immunoblotting using antibodies against V-ATPase subunit V1A (ATP6V1A), V1C1 (ATP6V1C1), or V0D (ATP6V0D). LAMP1 and GAPDH were used as loading controls for membrane proteins and cytosolic proteins, respectively. The levels of ATP6V0D in the membrane fraction are shown in (D) after normalization against LAMP1 ($n = 3$ independent experiments, ns represents non-significant). The levels of assembled ATP6V1A (E) ($n = 3$ independent experiments, *$P = 0.0118$, **$P = 0.0040$) and ATP6V1C1 (F) ($n = 3$ independent experiments, *$P = 0.0214$, **$P = 0.0013$) are normalized against ATP6V0D in the membrane fraction.

G Representative immunoblots for Ac-α-tubulin and GAPDH in the samples from (C).

H–K The assembly of V-ATPase V1-V0 holoenzymes in WT RPE1 cells over-expressing the α-tubulin deacetylase HDAC6 or EGFP as a control. Representative immunoblots for ATP6V0D, ATP6V1A, ATP6V1C1, LAMP1, and GAPDH are shown in (H). The levels of ATP6V0D in the membrane fraction (I) ($n = 3$ independent experiments, $P = 0.2602$) and those of assembled ATP6V1A (J) and ATP6V1C1 (K) ($n = 3$ independent experiments, *$P = 0.0101$, ***$P = 0.0008$) are quantified.

L Representative immunoblots for HDAC6, Ac-α-tubulin and GAPDH in the WT RPE1 cells over-expressing HDAC6 or EGFP.

M–O Loss of NDST3 enhances microtubule acetylation and the colocalization of the lysosomes with V-ATPase V1 subunits. WT and NDST3 KO RPE1 cells stably expressing LAMP1-GFP were fixed and analyzed by immunofluorescence staining with antibodies against ATP6V1C1 and Ac-α-tubulin. The relative levels of Ac-α-tubulin (N) ($n = 75$ cells in the WT group, $n = 79$ cells in the NDST3 KO group, ****$P < 0.0001$) and the colocalization of LAMP1-GFP with ATP6V1C1 (O) ($n = 75$ cells in the WT group, $n = 79$ cells in the NDST3 KO group, ****$P < 0.0001$) are quantified.

P–S The assembly of V-ATPase V1-V0 holoenzymes in NDST3 KO RPE1 cells over-expressing HDAC6 or EGFP as a control. Representative immunoblots for ATP6V0D, ATP6V1A, ATP6V1C1, LAMP1, and GAPDH are shown in (P). The levels of ATP6V0D in the membrane fraction relative to LAMP1 (Q) ($n = 3$ independent experiments, $P = 0.9795$) as well as the levels of assembled ATP6V1A (R) ($n = 3$ independent experiments, *$P = 0.0316$) and ATP6V1C1 (S) ($n = 3$ independent experiments, **$P = 0.0027$) are quantified.

T Representative immunoblots for HDAC6, Ac-α-tubulin and GAPDH in the NDST3 KO RPE1 cells over-expressing HDAC6 or EGFP.

Data information: Error bars represent ± standard deviation. Scale bar, 10 μm.
Source data are available online for this figure.

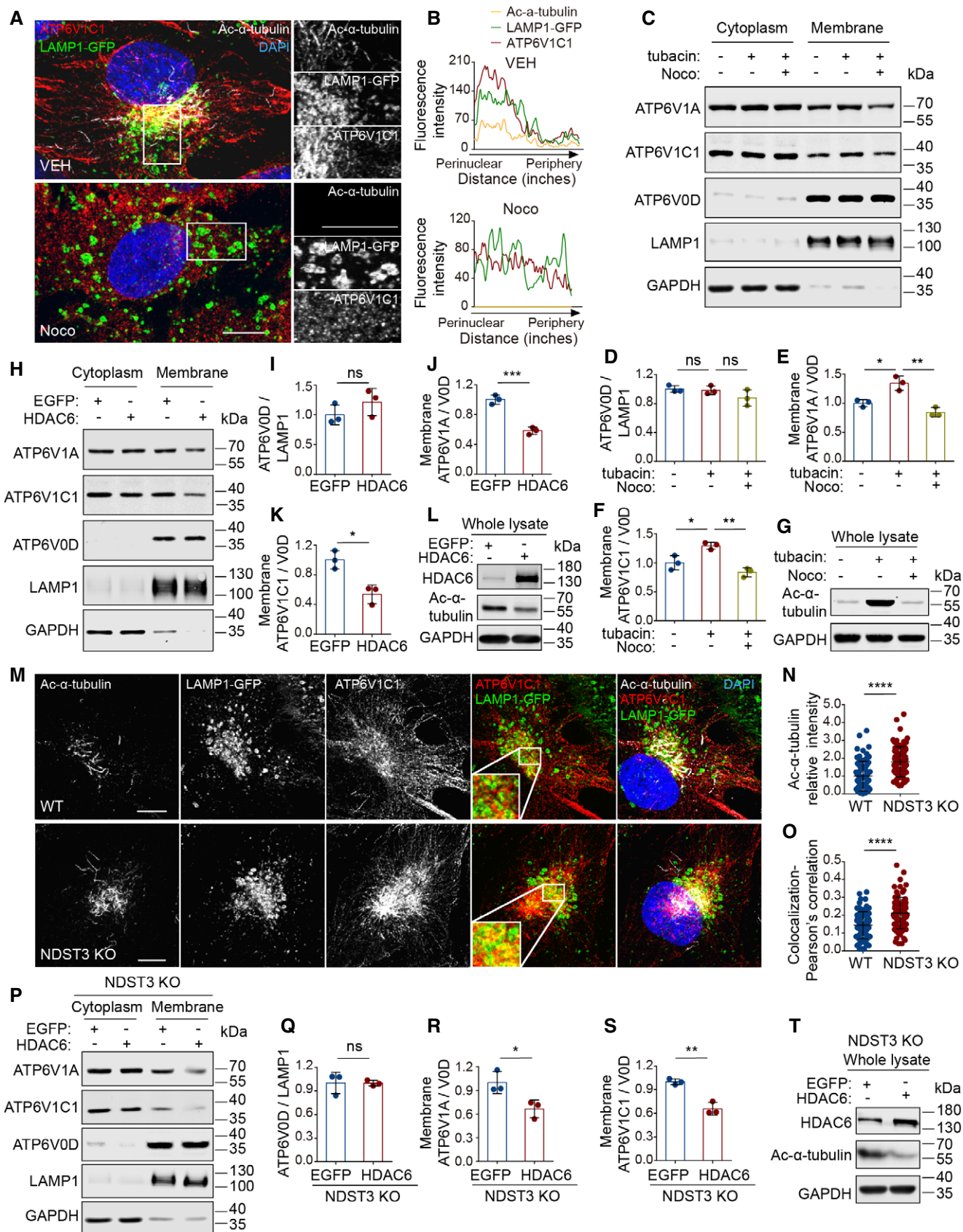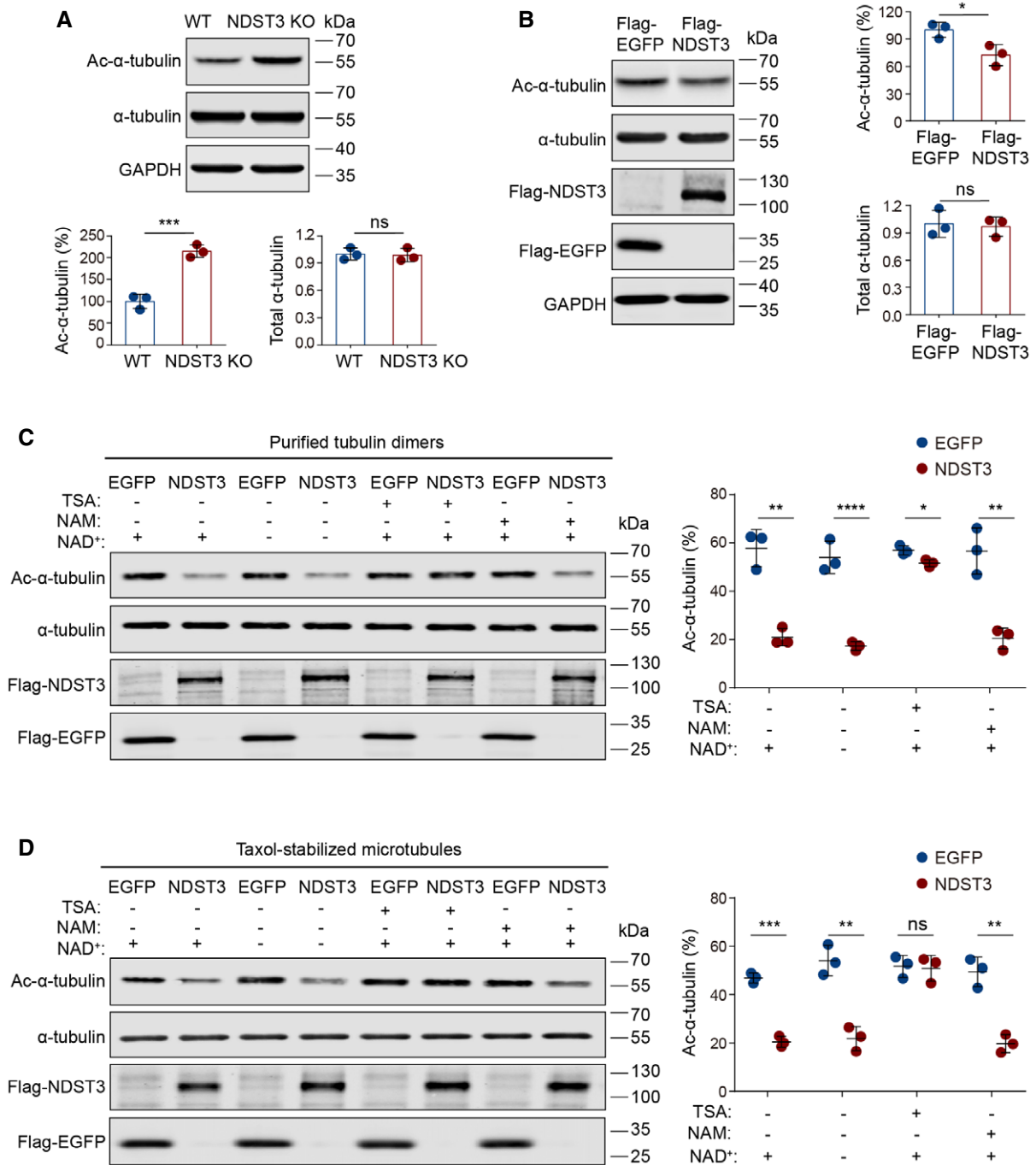Figure 4.

Figure 5. NDST3 deacetylates α-tubulin in the cells and *in vitro*.

A Immunoblotting analysis demonstrated a large accumulation of α-tubulin acetylated at Lys40 (Ac-α-tubulin) in NDST3 KO RPE1 cells, while the total α-tubulin relative to GAPDH remained unchanged (n = 3 independent cultures, ***P = 0.0008).

B Immunoblotting analysis showed decreased levels of Ac-α-tubulin, but unchanged levels of total α-tubulin relative to GAPDH, in RPE1 cells over-expressing Flag-NDST3 compared to those in Flag-EGFP control cells (n = 3 independent cultures, *P = 0.0399).

C *In vitro* enzymatic assay quantitating the effect of NDST3 on α-tubulin acetylation. Flag-NDST3 was expressed in HEK293T cells and immunoprecipitated by anti-Flag beads. Flag-EGFP was used as a control. The immunoprecipitated protein was incubated with purified tubulin heterodimers *in vitro*, with or without 1 mM NAD$^+$, 400 nM TSA, or 5 mM nicotinamide (NAM) for 2 h at room temperature. The reaction products were examined by immunoblotting against Ac-α-tubulin or total α-tubulin (n = 3 independent experiments, *P = 0.0185, **P < 0.01, ****P < 0.0001).

D The same *in vitro* enzymatic assay as in (C), except that the purified tubulin was polymerized in the presence of 20 μM Taxol and 1 mM GTP (n = 3 independent experiments, **P < 0.01, ***P = 0.0001).

Data information: Error bars represent ± standard deviation. ns means non-significant.
Source data are available online for this figure.

NDST3 is a deacetylase of α-tubulin

To study the mechanism through which loss of NDST3 increases the assembly of the V-ATPase holoenzyme, we explored the role of NDST3 in mediating microtubule acetylation. NDST3 was previously identified as a deacetylase of heparan sulfates (Grobe *et al*, 2002; Pallerla *et al*, 2008), prompting us to ask whether NDST3 can also deacetylate α-tubulin. Using immunoblotting assays, we found that the levels of α-tubulin acetylated at Lys40 were substantially increased in NDST3 KO cells when compared to WT cells, but the levels of total α-tubulin remained unchanged (Fig 5A). Conversely, when NDST3 was overexpressed in RPE1 cells, the level of α-tubulin acetylated at Lys40 was significantly lower than that in cells expressing the EGFP control (Fig 5B). Similar effects of NDST3 on α-tubulin deacetylation were observed in mouse N2a cells and N2a-differentiated neurons when NDST3 was knocked down with shRNA (Fig EV5A–F).

To test the deacetylase activity of NDST3 on α-tubulin directly, we performed an *in vitro* enzymatic assay. NDST3 protein was purified from HEK293T cells and incubated with purified tubulin heterodimers or polymers *in vitro*. The reaction products were examined by immunoblotting with a specific antibody against α-tubulin acetylated at Lys40. We found that the presence of NDST3, but not EGFP, led to robust deacetylation of α-tubulin in both the heterodimer and polymer forms (Fig 5C and D). The addition of nicotinamide adenine dinucleotide (NAD$^+$), a coenzyme required for the activity of Class III HDAC enzymes, did not alter the deacetylase activity of NDST3. Furthermore, the Class III HDAC inhibitor nicotinamide (NAM) did not show any inhibitory effect on NDST3 deacetylation *in vitro*. In contrast, trichostatin (TSA), an inhibitor of HDACs other than the Class III enzymes, reduced the catalytic activity of NDST3 on α-tubulin when the purified α-tubulin was present in the form of dimers (Fig 5C), and it completely inhibited the deacetylation when the α-tubulin was in the form of polymers (Fig 5D). These results demonstrate that NDST3 is a deacetylase of α-tubulin. Furthermore, the evidence suggests that NDST3 is a classical HDAC member rather than a Class III HDAC enzyme.

Implication of NDST3 in *C9orf72*-linked ALS

Given the critical role of NDST3 in the regulation of lysosomal functions, we explored its potential connection to neurodegenerative diseases with lysosome-related pathologies such as *C9orf72*-linked ALS. Immunoblot analysis of the protein levels of NDST3 in B lymphocytes from three ALS patients carrying *C9orf72* hexanucleotide repeat expansions and three healthy controls showed that NDST3 was significantly downregulated in the patients' cells when compared to those in the healthy controls (Fig 6A and B; Appendix Table S1). Moreover, the levels of NDST3 protein were significantly lower in the spinal cord tissues from five *C9orf72*-linked ALS patients than in those from four healthy controls (Fig 6C and D; Appendix Table S1). Consistent with the reduction of NDST3 and its role in microtubule acetylation, there was a significant increase in the levels of acetylated α-tubulin, but not the total α-tubulin, in the spinal cords from the ALS patients when compared to those from healthy controls (Fig 6C, E and F).

One of the consequences of the hexanucleotide repeat expansions is reduced expression of C9orf72 in patient cells and tissues. To address whether the reduction of NDST3 in the patient tissues is a result of the C9orf72 haploinsufficiency, we tested the regulation of NDST3 levels by C9orf72 using immunoblotting assays in cultured cells. When C9orf72 was knocked down in RPE1 cells, we found that NDST3 was significantly downregulated (Fig 6G–I). Conversely, when C9orf72 was overexpressed, NDST3 was significantly up-regulated (Fig 6J–L). These results indicate a positive regulation of C9orf72 on NDST3 protein levels.

Next, we asked whether NDST3 could affect the proteotoxicity associated with *C9orf72*-linked ALS. The proline-arginine (PR) poly-dipeptide is one of the toxic dipeptide repeat proteins produced via the non-AUG-dependent translation of the expanded *C9orf72* hexanucleotide repeat in ALS/FTD patients (Wen *et al*, 2014; Shi *et al*, 2017). To study the proteotoxicity of the PR poly-dipeptide, we expressed a codon-optimized construct producing a stretch of 82 repeats of the PR poly-dipeptide (PR82) in RPE1 cells and found that PR82 induced significantly higher cytotoxicity in NDST3 KO RPE1

Figure 6. NDST3 is downregulated in *C9orf72*-linked ALS patient cells and tissues.

A, B   NDST3 protein levels relative to β-tubulin in B lymphocytes derived from healthy controls and *C9orf72*-linked ALS patients, as examined by immunoblotting (*n* = 3 biologically independent samples, **P = 0.0026).

C–F   The protein levels of NDST3 relative to GAPDH (D) (**P = 0.0013), Ac-α-tubulin relative to total α-tubulin (E) (*P = 0.0379), and total α-tubulin relative to GAPDH (F) (P = 0.5700), as examined by immunoblotting, in spinal cord tissues from healthy controls and *C9orf72*-linked ALS patients (*n* = 4 biologically independent samples in the control group and *n* = 5 biologically independent samples in the ALS patient group).

G–I   Immunoblotting assays showing downregulation of NDST3 in *C9orf72* shRNA (shC9orf72)-treated RPE1 cells, as compared to control shRNA (shCTRL)-treated cells. Quantification of C9orf72 and NDST3 expression relative to GAPDH is shown in (H) (*n* = 4 independent experiments, ***P = 0.0004) and (I) (*n* = 4 independent experiments, ***P = 0.0001), respectively.

J–L   Immunoblotting assays showing up-regulation of NDST3 in RPE1 cells over-expressing Flag-C9orf72 compared to those expressing Flag-EGFP as control. Quantification of C9orf72 and NDST3 expression relative to GAPDH is shown in (K) (*n* = 3 independent experiments, **P = 0.0011) and (L) (*n* = 3 independent experiments, **P = 0.0033), respectively.

M, N   Baf A1 sensitivity assay for WT, NDST3 KO, and Noco-treated NDST3 KO RPE1 cells expressing proline-arginine poly-dipeptide (PR82). 24 h after the transfection of PR82, WT and NDST3 KO cells were treated with vehicle or 10 μg/ml Noco overnight. The cell survival measured using calcein AM staining at 48 h post-transfection was quantified as the percentage of the fluorescence intensity for treated cells relative to that of untreated cells (*n* = 3 independent cultures, *P = 0.0369, ***P = 0.0007). Scale bar, 200 μm.

O, P   Immunoblotting analysis of PR82 levels in WT, NDST3 KO, and Noco-treated NDST3 KO RPE1 cells from (M, N) after the drug treatment. Quantification of the levels of PR82 relative to β-tubulin is shown in (P) (*n* = 4 independent experiments, *P = 0.0141, **P = 0.0045).

Data information: Error bars represent ± standard deviation.
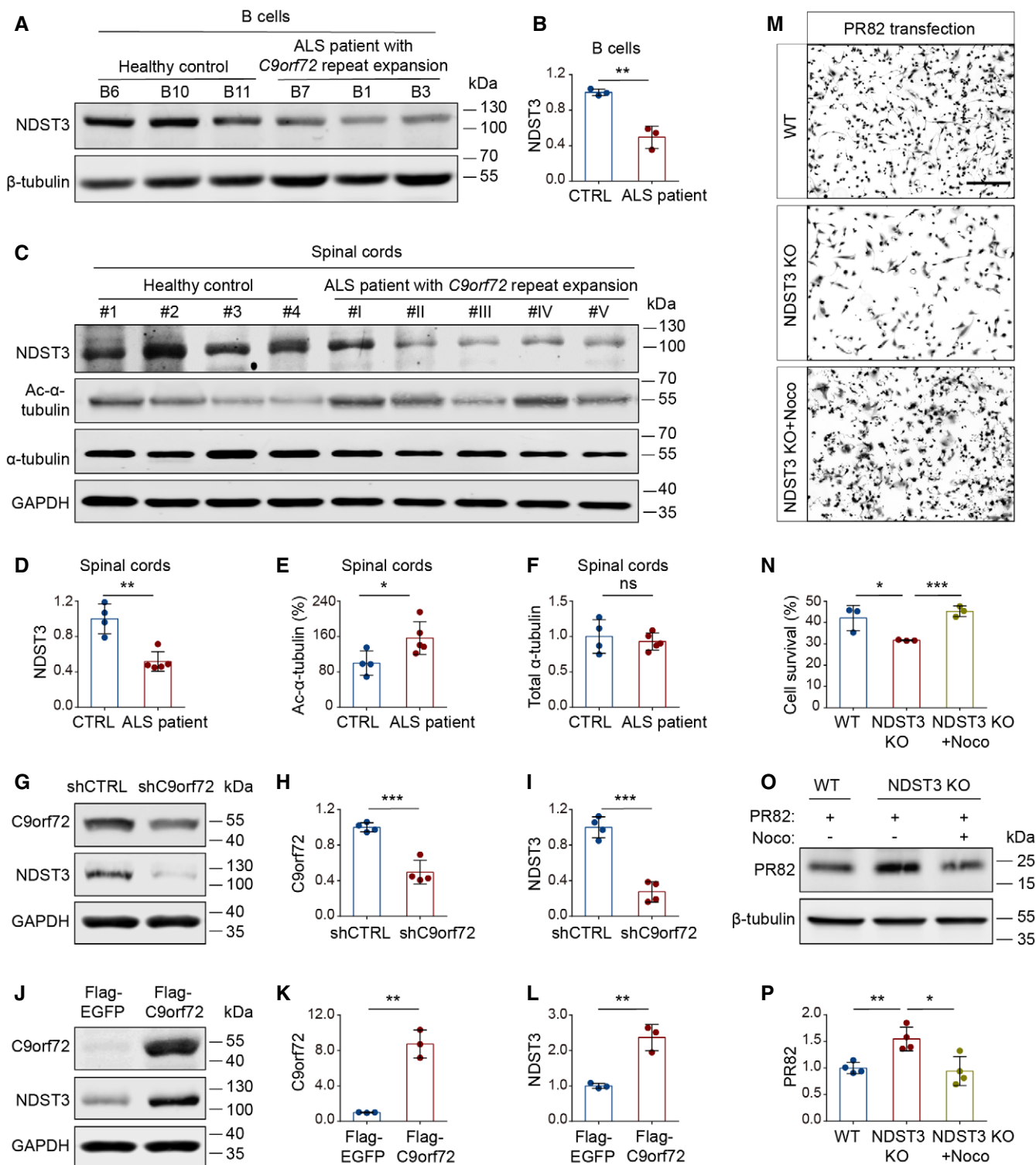Source data are available online for this figure.

Figure 6.

cells than in WT cells (Fig 6M and N). The immunoblotting results demonstrated a consistently increased level of the PR82 protein in NDST3 KO cells when compared to that in WT cells (Fig 6O and P). To determine whether the effect of NDST3 on PR82-induced

proteotoxicity was dependent on polymerized microtubules, we treated the PR82-expressing NDST3 KO cells with Noco to depolymerize the microtubules. The Noco treatment completely ablated the abnormal accumulation of PR82 in NDST3 KO cells (Fig 6O and

P) and slowed the cell death of NDST3 KO cells (Fig 6M and N). These observations suggest that the downregulation of NDST3 in *C9orf72*-linked ALS could contribute to the proteotoxicity in the disease through its functions related to microtubules and lysosomes.

Discussion

The autophagy-lysosomal pathway plays an essential role in maintaining normal cellular functions and is critically involved in human diseases ranging from cancer to neurodegeneration (Shu *et al*, 2020). Lysosomes, the first organelle discovered in this pathway, depend on an optimally maintained acidic lumenal environment in order to act as a functional degradation center. In the present study, we have identified a robust regulator of the autophagy-lysosomal pathway, NDST3, which regulates lysosomal acidification and degradative capacity through controlling V-ATPase assembly via a microtubule-dependent mechanism, where NDST3 acts as a previously uncharacterized deacetylase of α-tubulin (Fig 7).

NDST3 was previously recognized as a bifunctional enzyme that is responsible for catalyzing the N-deacetylation and N-sulfation of N-acetylglucosamine (GlcNAc) residues in heparan sulfate (Aikawa *et al*, 2001; Pallerla *et al*, 2008). Our *in vitro* and cell-based studies have now uncovered a new function for NDST3 as a deacetylase of α-tubulin. Evidence from our studies using inhibitors against various classes of deacetylases suggests that NDST3 is a classical HDAC member, rather than a Class III HDAC enzyme. Considering the key role of α-tubulin acetylation in maintaining microtubule stability (Portran *et al*, 2017; Eshun-Wilson *et al*, 2019), the identification of NDST3 as a α-tubulin deacetylase extends our understanding of the regulation of this critical post-translational modification and offers a new entry point for integrating signals that regulate microtubule integrity and associated functions.

The roles of microtubule deacetylation in the cell are not fully understood. The present study demonstrates that deficiency of microtubule deacetylation plays an important role in the regulation of V-ATPase holoenzymes. This finding provides a mechanistic link connecting NDST3 to the assembly of the V-ATPase holoenzyme on the lysosomal membrane as well as to the lysosome's acidification and degradative functions. We have demonstrated that loss of NDST3 promotes the acetylation of α-tubulin, the assembly of V-ATPase holoenzymes, and the acidification of the lysosomal lumen. In traditional models, an increase in lysosomal acidification would lead to an acceleration of the autophagic flux. However, we found that the over-acidification of the lysosome as a result of the loss of NDST3 led to an impairment of the lysosome's degradative activities, a decrease in the autophagic flux, and accumulation of misfolded proteins. These observations indicate that the maintenance of pH homeostasis within a normal range is required for the lysosome to optimally carry out its degradative activity. The lysosomal dysfunction may trigger a variety of downstream deleterious events, including apoptosis (Boya *et al*, 2005), accumulation of damaged organelles (Platt *et al*, 2012), and perturbation of iron homeostasis (Miles *et al*, 2017; Yambire *et al*, 2019; Weber *et al*, 2020), which could together lead to cell toxicity or death.

Our study also extends the association between NDST3 and human diseases. Previous genome-wide association studies have implicated NDST3 in psychiatric diseases such as schizophrenia and
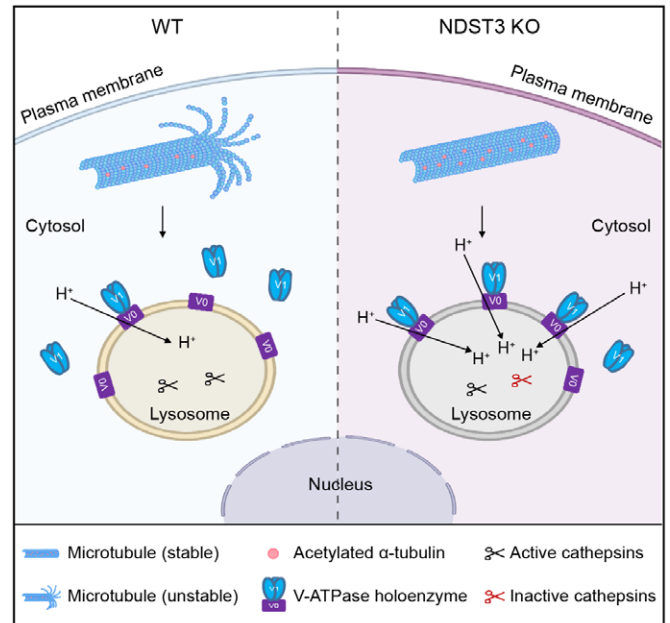

Figure 7. Schematic model for the role of NDST3 in the regulation of α-tubulin acetylation, V-ATPase assembly, and lysosomal functions.

Loss of NDST3 promotes α-tubulin acetylation and microtubule stability, increasing the level of the V-ATPase V1-V0 holoenzyme on lysosomal membranes and resulting in hyperacidification and dysfunction of the lysosomes.

bipolar disorder (Lencz *et al*, 2013; Gu *et al*, 2014; Sakai *et al*, 2015; Zhang *et al*, 2016). The present identification of NDST3 as a strong regulator of the autophagy-lysosomal pathway may implicate it in other neurological diseases. In particular, dysregulation of the autophagy-lysosomal pathway and associated proteostatic imbalance is a hallmark of neurodegenerative diseases (Martini-Stoica *et al*, 2016; Kurtishi *et al*, 2019). Notably, we now show that NDST3 is downregulated in the spinal cord tissues of ALS patients whose defects are linked to the hexanucleotide repeat expansion in *C9orf72*. Furthermore, we provide evidence that NDST3 deficiency leads to both accumulation of poly-dipeptides generated from the *C9orf72* hexanucleotide repeat expansion and exacerbation of their toxicity. These findings suggest that NDST3-dependent lysosomal dysregulations may contribute to the pathogenesis underlying *C9orf72*-linked ALS. In the present study, we have demonstrated that the regulatory effects of NDST3 on microtubule acetylation and lysosomal functions took place in neurons. Future studies are needed to fully understand the role of NDST3 in the complex interplay of the autophagy-lysosome pathway and the microtubule-meditated transport in different cell types including neurons relevant to the diseases. In summary, the present study has identified NDST3 as a previously unrecognized deacetylase of α-tubulin and has illustrated a pathway by which NDST3 regulates V-ATPase assembly and lysosomal functions. The findings of these NDST3 functions open new avenues for future studies such as developing therapeutic interventions to modulate microtubule acetylation and lysosomal acidification in the contexts of specific diseases.

Materials and Methods

Cell culture

Human retina pigmented epithelial (RPE1) cells immortalized with hTERT (ATCC CRL-4000) were cultured in DMEM-F12 complete growth medium supplemented with 10% FBS and 0.01 mg/ml hygromycin B. HEK293T cells (ATCC CRL-3216) and mouse Neuro-2a (N2a) cells (ATCC CCL-131) were cultured in DMEM supplemented with 10% FBS. For N2a differentiation, 8×10^4 N2a cells per well in 12-well plates were cultured in differentiation medium (DMEM + 2% FBS + 20 μM retinoic acid) for 48 h to be differentiated into neurons and used for subsequent experiments. All the cells were grown in a humidity-controlled incubator at 37°C with 5% CO_2.

Lentivirus production

HEK293T cells were cultured in PEI-coated dishes under standard culturing conditions. The lentiviral transfer plasmid encoding the insert of interest was co-transfected with the psPAX2 packaging plasmid (Addgene #12260) and the pMD2.G envelope plasmid (Addgene #12259) into HEK293T cells using Lipofectamine 2000 (Thermo Scientific #11668019) in OPTI-MEM medium to produce lentiviral particles. Lentiviral particle-containing medium was harvested at 60 h post-transfection, centrifuged at $500 \times g$ at 4°C for 10 min to pellet cell debris, and then filtered through a 0.45-μm PVDF membrane filter (Millipore Sigma HVHP02500). The harvested lentivirus was aliquoted and stored at −80°C.

Genome-wide CRISPR/Cas9 library screening

The CRISPR/Cas9 library screening was conducted in the RPE1 cells with the Human GeCKOv2 CRISPR Knockout pooled library, a gift from Feng Zhang (Addgene #1000000048), as previously described (Shalem *et al*, 2014). In brief, around 7.2×10^7 RPE1 cells were transduced with lentivirus particles containing the GeCKOv2 library A sgRNAs via spinfection. Twenty-four hours after the transduction, the infected cells underwent puromycin (10 μg/ml) selection for 5 days. The cells that survived the puromycin selection were then exposed to Baf A1 (100 nM, CST #54645) for 7 days, followed by a recovery to ~90% cell confluence. These treatment and recovery processes were repeated twice more. At the end of the screening, the surviving cells were passaged to another plate to harvest resistant colonies. The genomic DNAs from the cell colonies were extracted with a Blood & Cell Culture DNA Mini Kit (Qiagen #13323) and PCR-amplified for the lentiCRISPR sgRNAs. The resulting amplicons were gel-purified and subjected to Sanger sequencing (Genewiz, USA).

Generation of NDST3 knockout or knockdown cells

To generate knockout cells, RPE1 cells were infected with lentiviruses carrying either a *NDST3*-targeting sgRNA or a control sgRNA. The infected cells were selected with puromycin (10 μg/ml) for stable *NDST3* sgRNA expression. Single colonies were picked up to ensure the complete depletion of NDST3 in the cells. To genotype the NDST3 knockout cells, the genomic DNA was extracted, and the region around the targeting sgRNA was amplified by PCR (forward: CTAGATCTGTCTCACCACCC, reverse: CATACTGGAGGAAGCTCACC)

followed by Sanger sequencing. To generate knockdown cells, N2a cells were transfected with either *NDST3*-targeting shRNA (TRCN0000097828, Dharmacon) or a control shRNA expressed from the pLKO.1 vector. N2a-differentiated neurons were infected with lentivirus carrying either the *NDST3*-targeting shRNA or a control shRNA. After 72 h of knockdown treatments, the cells were used in subsequent experiments. The gene expression levels were measured by quantitative RT–PCR (NDST3 forward: CCAATGATG-TAAAGGCCCTGC, NDST3 reverse: TCTGAAGTCGCAGGTTGGTC, GAPDH forward: GAGTCAACGGATTTGGTCGT, GAPDH reverse: TTGATTTTGGAGGGATCTCG).

Cell survival assay

After the treatment of either Baf A1 exposure or proline-arginine poly-dipeptide overexpression, cell viability was analyzed using calcein AM (Invitrogen #C3099), a cell-permeant fluorescent dye for live cell staining. In brief, cells were plated in either a 6-well plate or 12-well plate at ~60% confluence and subjected to the specific treatment. Blank control (containing calcein AM but no cells) and positive control (containing cells but without treatment) wells were used to determine the background signal and the total number of cells for each group, respectively. Following the treatment, the cell culture medium was removed, and cells were gently washed with 1× DPBS (containing $MgCl_2$ and $CaCl_2$). The cells were then incubated with either 600 μl (for a 12-well plate) or 1 ml (for a 6-well plate) per well of 3 μM calcein AM at 37°C for 30 min. Finally, the fluorescence intensity in the wells was detected at 485 nm/535 nm (excitation/emission) using a plate reader (BioTek, Synergy H1) and a fluorescence microscope was used for imaging (Nikon Eclipse TS100, equipped with Lumencor). The fluorescence intensity of the experimental wells, blank control wells, and positive control wells was recorded as F_x, F_0, and F_{max}, respectively. The cell survival percentage of the experimental wells was calculated with the following equation: $\text{Cell survival}\,(\%) = (F_x - F_0)/(F_{max} - F_0) \times 100$.

Generation of anti-NDST3 polyclonal antibody

By comparing the protein sequence of NDST3 with its family members NDST1, NDST2, and NDST4, we found a region (aa 52–73, CGDLQHLPYQLMEVKAMKLFDA) in NDST3 with relatively low homology to the other NDSTs. Therefore, we designed an antigen using this segment of protein sequence. The synthesis and immunization of the antigen as well as the purification of antibodies were performed by 21st Century Biochemicals. The specificity of the chosen polyclonal antibody was validated using NDST3 KO cells.

2D-CN/SDS–PAGE electrophoresis

Two dimensional (2D)-clear native (CN)/SDS–PAGE electrophoresis was performed to analyze the NDST3 protein level. For the preparation of protein samples, cells were lysed in ice-cold 1× native cell lysis buffer (CST #9803) for 5 min and sonicated on ice three times for 5 s each. The cell lysates were then centrifuged, and the supernatant was mixed with a native sample buffer (Bio-Rad #161-0738) before being loaded onto the first-dimension gel. The first-dimension electrophoresis was a clear native PAGE. The proteins were separated in a precast 4–20% mini-protean TGX PAGE gel

(Bio-Rad #4561095) by charge-to-mass ratio. After the first-dimension separation at a low voltage on ice, the gel was cut into strips lane by lane and equilibrated in the SDS–PAGE buffer for 30 min. The strips were then applied in the second-dimension separation using SDS–PAGE after being rotated 90° counter-clockwise. The second-dimension electrophoresis separated the proteins a second time by molecular weight. The subsequent procedure was the same as that in the immunoblotting analysis. The antibodies used in the 2D-CN/SDS–PAGE electrophoresis were rabbit polyclonal anti-NDST3 (1:500, generated in-house), rabbit polyclonal anti-NDST3 (1:500, Abcam #ab173356), rabbit monoclonal anti-GAPDH (1:1,000, CST #2118), and goat anti-rabbit IgG (H + L) (DyLight 680 conjugate) (1:10,000, CST #5366).

NDST3 ORF cloning

A cDNA library of RPE1 cells was used as a template for the cloning of the NDST3 open reading frame (ORF). PCR was conducted for 20 cycles using Phusion High-Fidelity DNA Polymerase (NEB M0530L), with the forward primer GGGGACAAGTTTGTACAAAAAAGCAGGC-TAGTCAAAAAGCCTGAGCCGATG and the reverse primer GGGGAC-CACTTTGTACAAGAAAGCTGGGTCTGCCTTTTGGTAGCTTCTGG, containing an attB1 and an attB2 sequence, respectively. The resulting amplicon was gel-extracted and inserted into a Gateway pDONR221 vector (Thermo Fisher Scientific #12536017) and then cloned into either a lentiviral vector (pLenti6.2-ccdB-3×Flag-V5, Addgene #87071) or a pcDNA3.1-CMV-3×nFlag vector using a Gateway Single-Fragment BP/LR reaction. In addition, for the rescue experiment, because of the remaining expression of the sgRNA and Cas9 in the NDST3 KO cells, synonymous mutations were created for the NDST3 ORF at the sgRNA-targeted region by replacing several base pairs with nucleotides encoding the same amino acids using a Q5 Site-Directed Mutagenesis Kit (NEB E0554) to render the NDST3 cDNA resistant to cleavage.

Immunoblotting and antibodies

Cell lysates were prepared with RIPA lysis buffer supplemented with 1 mM PSMF (CST #8553), protease inhibitor cocktail (1:100, CST #5871), 10 μM TSA (CST #9950S), and 10 mM NAM (Sigma-Aldrich N0636). Protein concentrations were determined by the Pierce BCA protein assay. The antibodies used are as follows: rabbit polyclonal anti-NDST3 (1:500, generated in-house), rabbit polyclonal anti-β-tubulin (1:4,000, Proteintech #10068-1-AP), mouse monoclonal anti-Flag (1:1,000, Millipore Sigma F3165), rabbit monoclonal anti-LAMP1 (1:1,000, CST #9091), mouse monoclonal anti-β-actin (1:1,000, Santa Cruz sc-47778), rabbit monoclonal anti-LC3B (1:1,000, CST #3868), rabbit monoclonal anti-p62 (1:1,000, CST #5114), rabbit monoclonal anti-GAPDH (1:1,000, CST #2118), rabbit monoclonal anti-Cathepsin B (1:1,000, CST #31718), mouse monoclonal anti-ATP6V1A (1:500, Santa Cruz sc-293336), mouse monoclonal anti-ATP6V1C1 (1:500, Santa Cruz sc-271077), mouse monoclonal anti-ATP6V0D (1:500, Santa Cruz sc-393322), rabbit monoclonal anti-vinculin (1:1,000, CST #13901), mouse monoclonal anti-α-tubulin (1:500, Santa Cruz sc-23948), mouse monoclonal anti-acetylated-α-tubulin (Lys40, 1:500, Santa Cruz sc-23950), rabbit monoclonal anti-HDAC6 (1:1,000, CST #7558), mouse monoclonal anti-C9orf72 (1:500, Bio-Rad VMA00065), rabbit polyclonal anti-PR repeat (1:1,000, Proteintech #23979-1-AP), IRDye 680LT goat anti-rabbit IgG secondary antibody (1:10,000, LI-COR #926-68021), IRDye 800CW goat anti-rabbit IgG secondary antibody (1:10,000, LI-COR #926-32211), IRDye 680LT donkey anti-mouse IgG secondary antibody (1:10,000, LI-COR #926-68022), and IRDye 800CW donkey anti-mouse IgG secondary antibody (1:10,000, LI-COR #926-32212). Immunoblots were analyzed for band intensity with a LI-COR Odyssey CLx Infrared Imaging System (LI-COR, USA).

Immunocytochemistry

Cells were grown on coverslips to ~80% confluence. After the treatment with relevant drugs, the culture medium was aspirated and the cells were fixed with 4% PFA. Following three times of 1× PBS washes, the fixed cells were blocked with blocking buffer (1× PBS / 5% BSA / 0.3% Triton X-100) for 1 h at room temperature. After the aspiration of blocking solution, the cells were stained with relevant primary and secondary antibodies. The primary antibodies used are as follows: rabbit monoclonal anti-LAMP1 (1:200, CST #9091S), rabbit monoclonal anti-acetyl-α-tubulin (Lys40) (1:800, CST #5335T), mouse monoclonal anti-ATP6V1C1 (1:50, Santa Cruz sc-271077), goat polyclonal anti-Cathepsin B (5 μg/ml, R&D Systems AF953), and rabbit polyclonal anti-β-tubulin (1:500, Proteintech #10068-1-AP). The coverslips were mounted with ProLong Diamond Antifade Mountant with DAPI (Invitrogen P36962) after PBS washes. Images were acquired using a confocal microscope (Leica, TCS SP8), and fluorescence intensity of puncta was quantified using Fiji software.

LysoTracker staining

The LysoTracker staining was performed on live cells as described previously (Chazotte, 2011). Stable LAMP1-GFP RPE1 cell lines were generated with the pLVX-EF1a-LAMP-1-mGFP-IRES-Puromycin plasmid (Addgene #134868, a gift from David Andrews) (Schormann et al, 2020). Then, the cells were grown on coverslips in normal culture medium to ~80% confluence. The LysoTracker Red DND-99 probe (Invitrogen L7528) was diluted to a working concentration of 50 nM in pre-warmed (37°C) culture medium and applied to replace the normal culture medium. After the cells were incubated with the probe-containing medium for 1 h under growth conditions, the loading medium was aspirated, and the cells were washed with fresh normal culture medium to remove any extra dye from the coverslips. The nucleus was stained with Hoechst 33342 (ImmunoChemistry #639) at a concentration of 0.5% v/v. The coverslips were then transferred onto slides and mounted with PBS. The slides were imaged immediately under a confocal microscope (Leica, TCS SP8). The number and size of LysoTracker-positive puncta per cell were quantified. The colocalization of LysoTraker and LAMP1-GFP was analyzed using the colocalization tool in Fiji software.

Lysosomal pH measurements

The lysosomal pH values in WT and NDST3 KO RPE1 cells were measured as described previously (Lee et al, 2010; Guha et al, 2014) using ratiometric probes including LysoSensor Yellow/Blue dextran (Invitrogen L22460) and LysoSensor Yellow/Blue DND-160 (Invitrogen L7545). WT and NDST3 KO RPE1 cells were grown either on coverslips or in black 96-well plates to confluence. For the LysoSensor Yellow/Blue dextran staining, cells were incubated,

protected from light, with 1 mg/ml LysoSensor Yellow/Blue dextran for 24 h under normal culture conditions before treatment with selected drugs. For the LysoSensor Yellow/Blue DND-160 staining, cells were treated with drugs followed by removal of the culture medium, and the cells were incubated, protected from light, with 2 µM LysoSensor Yellow/Blue DND-160 for 3 min at room temperature in an isotonic buffer (105 mM NaCl, 5 mM KCl, 6 mM HEPES-Acid, 4 mM HEPES-Na, 5 mM NaHCO$_3$, 60 mM mannitol, 5 mM glucose, 0.5 mM MgCl$_2$, 1.3 mM CaCl$_2$, adjusted to pH 7.4). Immediately after the staining, cells were rinsed with isotonic buffer three times to remove the extra dye.

The coverslips were mounted with PBS and then observed and imaged immediately under a confocal microscope (Leica, TCS SP8). The excitation wavelength was set to ~405 nm. Images were captured under both emission wavelengths, 450 ± 33 nm and 510 ± 20 nm. The fluorescence intensity in black 96-well plates was determined with a plate reader (BioTek, Synergy H1) at dual excitation wavelengths, 340 nm ($F_{340\,nm}$) and 380 nm ($F_{380\,nm}$), with the emission wavelength set at 527 nm. Relative lysosomal pH was determined from the $F_{340\,nm}/F_{380\,nm}$ ratio.

To obtain the absolute lysosomal pH value, calibrations were performed using a series of pH calibration buffers (pH 4.0, 4.5, 5.0, 5.5, 6.0, and 6.5) in MES solution (20 mM 2-(N-morpholino) ethanesulfonic acid, 110 mM KCl, 20 mM NaCl). RPE1 cells were incubated with calibration buffers in the presence of 10 µM monensin and 30 µM nigericin at room temperature for 10 min after staining with the ratiometric probes. The fluorescence intensity ratios ($F_{340\,nm}/F_{380\,nm}$) were calculated for the pH-calibrated cells. A lysosomal pH calibration curve was then drawn by using both the pH values and the fluorescence intensity ratios.

Lysosome isolation

Lysosomes were isolated using the Lysosome Enrichment Kit for Tissues and Cultured Cells (Thermo Scientific #89839). In brief, cell pellets were lysed and neutralized with PSMF and protease inhibitors, and centrifuged at $500 \times g$ for 10 min at 4°C. The supernatant was collected and subjected to ultracentrifugation in discontinuous density gradients at $145,000 \times g$ for 2 h at 4°C. After centrifugation, the lysosome fraction at the top of the gradient was collected and washed with 1× PBS. The lysosome pellet was saved at −80°C for subsequent experiments.

Cathepsin activity assay

Cathepsin B activity was measured with ICT's Magic Red Cathepsin B substrate MR-(RR)$_2$ (ImmunoChemistry #6134). In brief, cells were seeded onto coverslips and grown to 60–70% confluence. The MagicRed probe was first diluted in H$_2$O at a ratio of 1:10 and then added into the cell culture medium at approximately 1:26. The cells were incubated with the probe for 1 h at 37°C and protected from light. Cells were cleared of the medium and washed twice for 1 min with 1× DPBS. Subsequently, the cells were stained with Hoechst 33342 (ImmunoChemistry #639) at a concentration of 0.5% v/v. The coverslips were mounted with a drop of PBS, and the cells were immediately observed for MagicRed-stained puncta by confocal microscopy. The MagicRed intensity per cell was analyzed using Fiji software.

In vitro Cathepsin B maturation assay

The recombinant human Cat B (BioLegend #557702) was diluted to 10 µg/ml in activation buffers (25 mM MES, 1 mM DTT) with different pH values (4.0, 4.5, 5.0, 5.5, 6.0, and 6.5) and incubated at 25°C for 10 min. The incubation was terminated by the addition of 5× SDS–PAGE protein loading buffer and boiled at 95°C for 10 min. The samples were then subjected to immunoblotting assays. The ratio of mature Cat B to proCat B was calculated to evaluate the maturation rate of Cat B.

Dextran degradation assay

Cells were grown on coverslips to 60–80% confluence and loaded with 0.4 mg/ml Alexa Fluor 488-dextran (10,000 MW, Invitrogen D22910) for 20 min in culture medium as previously described (Liu *et al*, 2018). Following aspiration of the culture medium, cells were washed twice with PBS to remove the un-endocytosed dextran. Subsequently, the cell samples for uptake analyses were immediately fixed with 4% PFA, and the other parallel samples for chase analyses were incubated in normal culture medium for 4 h and then fixed with 4% PFA after culture medium removal. Drug treatment was carried out during the chase period. The coverslips were mounted with ProLong Diamond Antifade Mountant with DAPI (Invitrogen P36962). Images were acquired using a confocal microscope (Leica, TCS SP8) with the excitation wavelength set at ~488 nm and emission wavelength at 520 ± 20 nm. Fluorescence intensity was quantified using Fiji software. The fluorescence intensity of the uptake and the chase was recorded as F_{uptake} and F_{chase}, respectively. The degradation of Alexa Fluor 488-dextran was calculated with the following equation: Degradation $(\%) = (F_{uptake} - F_{chase})/F_{uptake} \times 100$.

Subcellular fractionation

Subcellular fractionation was conducted with the Cell Fractionation Kit (CST #9038). In brief, cells grown to 80–90% confluence in 10-cm dishes were cleared of medium and washed with 1× DPBS, followed by extraction with ice-cold Cytosol Isolation Buffer (CIB, 300 µl) supplemented with 1 mM PSMF (CST #8553), protease inhibitor cocktail (1:100, CST #5871), 10 µM trichostatin A (TSA, CST #9950S), and 10 mM nicotinamide (NAM, Sigma-Aldrich N0636). The tubes were vortexed for 5 s and then incubated on ice for 5 min. The extracts were centrifuged at $500 \times g$ for 5 min, and the supernatants were saved as the cytosolic fractions. The pellets were resuspended in 200 µl ice-cold Membrane Isolation Buffer (MIB), which was also supplemented with inhibitors equivalent to those in the CIB. The mixtures were vortexed for 15 s, incubated on ice for 5 min, and centrifuged at $8,000 \times g$ for 5 min. The supernatants were saved as the membrane fractions. The subcellular fractions were mixed with SDS loading buffer and boiled at 95°C for 5 min for subsequent immunoblotting analysis.

Purification of NDST3 protein

NDST3 was overexpressed in HEK293T cells by transfecting the cells with the pcDNA3.1-CMV-3×nFlag-NDST3 plasmid. At 48 h post-transfection, HEK293T cells were harvested and lysed in ice-cold lysis buffer (50 mM Tris–HCl [pH 7.5], 0.5 mM EDTA, 0.5% NP-40,

150 mM NaCl, 1 mM PMSF, and 1× protease inhibitor cocktail). Cell lysates were precleared and immunoprecipitated with Anti-FLAG M2 Magnetic Beads (Sigma-Aldrich M8823). The immunoprecipitated Flag fusion protein was eluted with 3× Flag peptides (Sigma-Aldrich F4799). The Flag-tagged EGFP control protein was also prepared by the same method.

In vitro α-tubulin deacetylation assay

The *in vitro* α-tubulin deacetylation assay was performed as described previously (Hubbert *et al*, 2002; North *et al*, 2003). In brief, purified NDST3 or EGFP protein was added in 100 µl deacetylation buffer (10 mM Tris–HCl [pH 8.0] and 10 mM NaCl), together with either purified dimeric tubulin (Cytoskeleton Inc. T240) or Taxol-stabilized polymerized microtubules that had been assembled from the dimeric tubulin in PEM buffer (80 mM PIPES [pH 6.8], 1 mM $MgCl_2$, and 1 mM EGTA) supplemented with 20 µM Taxol (MilliporeSigma T7402) and 1 mM GTP (MilliporeSigma G8877) at 37°C for 30 min. The experimental reaction was performed at 25°C for 2 h in either the presence or absence of 1 mM NAD (MilliporeSigma N6522), with constant stirring. Inhibitory controls were also prepared using the histone deacetylase inhibitors TSA (CST #9950S) or NAM (Sigma-Aldrich N0636). TSA or NAM was added to the reaction system before the addition of substrate and NAD at a final concentration of 400 nM and 5 mM, respectively. After incubation at 25°C for 10 min, the reaction was started, following the same procedure as in the experimental reaction. All deacetylation reactions were stopped by the addition of 50 µl 5× SDS–PAGE loading buffer, and the samples were subjected to immunoblotting analysis to measure the acetylated-α-tubulin level.

Statistical analysis

All data were derived from at least three independent experiments. The exact *n* value for each data set used for calculating statistics is indicated in the corresponding figure legend. Data are expressed as mean ± standard deviation (SD). The two-tailed Student's *t*-test was used to analyze the data unless otherwise indicated. A *P* value of < 0.05 was considered statistically significant.

Data availability

This study includes no data deposited in external repositories.

Expanded View for this article is available online.

Acknowledgements

Author contributions

Conflict of interest

The authors declare that they have no conflict of interest.

References

Abbas YM, Wu D, Bueler SA, Robinson CV, Rubinstein JL (2020) Structure of V-ATPase from the mammalian brain. *Science* 367: 1240–1246

Aikawa J, Grobe K, Tsujimoto M, Esko JD (2001) Multiple isozymes of heparan sulfate/heparin GlcNAc N-deacetylase/GlcN N-Sulfotransferase structure and activity of the fourth member, NDST4. *J Biol Chem* 276: 5876–5882

Boya P, González-Polo R-A, Casares N, Perfettini J-L, Dessen P, Larochette N, Métivier D, Meley D, Souquere S, Yoshimori T *et al* (2005) Inhibition of macroautophagy triggers apoptosis. *Mol Cell Biol* 25: 1025–1040

Breton S, Brown D (2013) Regulation of luminal acidification by the V-ATPase. *Physiology* 28: 318–329

Chazotte B (2011) Labeling lysosomes in live cells with LysoTrackerLabeling lysosomes in live cells with LysoTracker. *Cold Spring Harb Protoc* 2011: pdb.prot5571

Chung CY, Shin HR, Berdan CA, Ford B, Carl C, Olzmann JA, Zoncu R, Nomura DK (2019) Covalent targeting of the vacuolar H+-ATPase activates autophagy via mTORC1 inhibition. *Nat Chem Biol* 15: 776–785

Dehay B, Ramirez A, Martinez-Vicente M, Perier C, Canron MH, Doudnikoff E, Vital A, Vila M, Klein C, Bezard E (2012) Loss of P-type ATPase ATP13A2/PARK9 function induces general lysosomal deficiency and leads to Parkinson disease neurodegeneration. *Proc Natl Acad Sci USA* 109: 9611–9616

DeJesus-Hernandez M, Mackenzie I, Boeve B, Boxer A, Baker M, Rutherford N, Nicholson A, Finch NiCole A, Flynn H, Adamson J *et al* (2011) Expanded GGGGCC hexanucleotide repeat in noncoding region of C9ORF72 causes chromosome 9p-linked FTD and ALS. *Neuron* 72: 245–256

Deriy LV, Gomez EA, Jacobson DA, Wang X, Hopson JA, Liu XY, Zhang G, Bindokas VP, Philipson LH, Nelson DJ (2009) The granular chloride channel ClC-3 is permissive for insulin secretion. *Cell Metab* 10: 316–323

Eshun-Wilson L, Zhang R, Portran D, Nachury MV, Toso DB, Löhr T, Vendruscolo M, Bonomi M, Fraser JS, Nogales E (2019) Effects of α-tubulin acetylation on microtubule structure and stability. *Proc Natl Acad Sci USA* 116: 10366–10371

Forgac M (2007) Vacuolar ATPases: rotary proton pumps in physiology and pathophysiology. *Nat Rev Mol Cell Biol* 8: 917–929

Gan L, Ye S, Chu A, Anton K, Yi S, Vincent VA, von Schack D, Chin D, Murray J, Lohr S *et al* (2004) Identification of cathepsin B as a mediator of neuronal death induced by Aβ-activated microglial cells using a functional genomics approach. *J Biol Chem* 279: 5565–5572

Gatica D, Lahiri V, Klionsky DJ (2018) Cargo recognition and degradation by selective autophagy. *Nat Cell Biol* 20: 233–242

Grobe K, Ledin J, Ringvall M, Holmborn K, Forsberg E, Esko JD, Kjelle L (2002) Heparan sulfate and development: differential roles of the N-acetylglucosamine N-deacetylase/N-sulfotransferase isozymes. *Biochim Biophys Acta* 1573: 209–215

Gu L-Z, Jiang T, Cheng Z-H, Zhang Y-C, Ou M-M, Chen M-C, Zhou Z-H, Ling W-M (2014) rs11098403 polymorphism near NDST3 is associated with a reduced risk of schizophrenia in a Han Chinese population. *Neurosci Lett* 581: 42–45

Guha S, Coffey EE, Lu W, Lim JC, Beckel JM, Laties AM, Boesze-Battaglia K, Mitchell CH (2014) Approaches for detecting lysosomal alkalinization and impaired degradation in fresh and cultured RPE cells: evidence for a role in retinal degenerations. *Exp Eye Res* 126: 68–76

Haeusler AR, Donnelly CJ, Periz G, Simko EAJ, Shaw PG, Kim M-S, Maragakis NJ, Troncoso JC, Pandey A, Sattler R *et al* (2014) C9orf72 nucleotide repeat structures initiate molecular cascades of disease. *Nature* 507: 195–200

Hubbert C, Guardiola A, Shao R, Kawaguchi Y, Ito A, Nixon A, Yoshida M, Wang X-F, Yao T-P (2002) HDAC6 is a microtubule-associated deacetylase. *Nature* 417: 455–458

Janke C, Montagnac G (2017) Causes and consequences of microtubule acetylation. *Curr Biol* 27: R1287–R1292

Ji YJ, Ugolino J, Zhang T, Lu J, Kim D, Wang J (2020) C9orf72/ALFA-1 controls TFEB/HLH-30-dependent metabolism through dynamic regulation of Rag GTPases. *PLoS Genet* 16: e1008738

Kane PM (2000) Regulation of V-ATPases by reversible disassembly. *FEBS Lett* 469: 137–141

Katoh Y, Michisaka S, Nozaki S, Funabashi T, Hirano T, Takei R, Nakayama K (2017) Practical method for targeted disruption of cilia-related genes by using CRISPR/Cas9-mediated, homology-independent knock-in system. *Mol Biol Cell* 28: 898–906

Kiselyov K, Muallem S (2008) Mitochondrial Ca2+ homeostasis in lysosomal storage diseases. *Cell Calcium* 44: 103–111

Klionsky DJ, Abdelmohsen K, Abe A, Abedin J, Abeliovich H, Bartolom A, Beckham JD, Bertolotti A, Bess AS, Bozhkov PV *et al* (2016) Guidelines for the use and interpretation of assays for monitoring autophagy (3rd edition). *Autophagy* 12: 1–222

Kurtishi A, Rosen B, Patil KS, Alves GW, Møller SG (2019) Cellular proteostasis in neurodegeneration. *Mol Neurobiol* 56: 3676–3689

Lawrence RE, Zoncu R (2019) The lysosome as a cellular centre for signalling, metabolism and quality control. *Nat Cell Biol* 21: 133–142

Lee J-H, Yu WH, Kumar A, Lee S, Mohan PS, Peterhoff CM, Wolfe DM, Martinez-Vicente M, Massey AC, Sovak G *et al* (2010) Lysosomal proteolysis and autophagy require presenilin 1 and are disrupted by Alzheimer-related PS1 mutations. *Cell* 141: 1146–1158

Lencz T, Guha S, Liu C, Rosenfeld J, Mukherjee S, DeRosse P, John M, Cheng L, Zhang C, Badner JA *et al* (2013) Genome-wide association study implicates NDST3 in schizophrenia and bipolar disorder. *Nat Commun* 4: 2739

Liu B, Palmfeldt J, Lin L, Colaço A, Clemmensen KKB, Huang J, Xu F, Liu X, Maeda K, Luo Y *et al* (2018) STAT3 associates with vacuolar H + -ATPase and regulates cytosolic and lysosomal pH. *Cell Res* 28: 996–1012

Mach L, Mort JS, Glossl J (1994) Maturation of human procathepsin B. Proenzyme activation and proteolytic processing of the precursor to the mature proteinase, in vitro, are primarily unimolecular processes. *J Biol Chem* 269: 13030–13035

Martini-Stoica H, Xu Y, Ballabio A, Zheng H (2016) The autophagy-lysosomal pathway in neurodegeneration: a TFEB perspective. *Trends Neurosci* 39: 221–234

Matteoni R, Kreis TE (1987) Translocation and clustering of endosomes and lysosomes depends on microtubules. *J Cell Biol* 105: 1253–1265

Mauthe M, Orhon I, Rocchi C, Zhou X, Luhr M, Hijlkema K-J, Coppes RP, Engedal N, Mari M, Reggiori F (2018) Chloroquine inhibits autophagic flux by decreasing autophagosome-lysosome fusion. *Autophagy* 14: 1435–1455

Mauvezin C, Nagy P, Juhász G, Neufeld TP (2015) Autophagosome–lysosome fusion is independent of V-ATPase-mediated acidification. *Nat Commun* 6: 7007

Maxson ME, Grinstein S (2014) The vacuolar-type H+-ATPase at a glance–more than a proton pump. *J Cell Sci* 127: 4987–4993

Miles AL, Burr SP, Grice GL, Nathan JA (2017) The vacuolar-ATPase complex and assembly factors, TMEM199 and CCDC115, control HIF1α prolyl hydroxylation by regulating cellular Iron levels. *Elife* 6: e22693

Mindell JA (2012) Lysosomal acidification mechanisms. *Annu Rev Physiol* 74: 69–86

Mizushima N, Yoshimori T, Levine B (2010) Methods in mammalian autophagy research. *Cell* 140: 313–326

Nguyen DKH, Thombre R, Wang J (2019) Autophagy as a common pathway in amyotrophic lateral sclerosis. *Neurosci Lett* 697: 34–48

Nixon RA (2020) The aging lysosome: An essential catalyst for late-onset neurodegenerative diseases. *Biochim Biophys acta Proteins Proteomics* 1868: 140443

North BJ, Marshall BL, Borra MT, Denu JM, Verdin E (2003) The human Sir2 ortholog, SIRT2, is an NAD+-dependent tubulin deacetylase. *Mol Cell* 11: 437–444

O'Rourke JG, Bogdanik L, Yáñez A, Lall D, Wolf AJ, Muhammad AKMG, HO R, Carmona S, Vit JP, Zarrow J *et al* (2016) C9orf72 is required for proper macrophage and microglial function in mice. *Science* 351: 1324–1329

Pallerla SR, Lawrence R, Lewejohann L, Pan Y, Fischer T, Schlomann U, Zhang X, Esko JD, Grobe K (2008) Altered heparan sulfate structure in mice with deleted NDST3 gene function. *J Biol Chem* 283: 16885–16894

Piao S, Amaravadi RK (2016) Targeting the lysosome in cancer. *Ann N Y Acad Sci* 1371: 45–54

Platt FM, Boland B, van der Spoel AC (2012) Lysosomal storage disorders: the cellular impact of lysosomal dysfunction. *J Cell Biol* 199: 723–734

Portran D, Schaedel L, Xu Z, Nachury MV, Physiology C (2017) Tubulin acetylation protects long-lived microtubules against mechanical aging. *Nat Cell Biol* 19: 391–398

Renton A, Majounie E, Waite A, Simón-Sánchez J, Rollinson S, Gibbs J, Schymick J, Laaksovirta H, van Swieten J, Myllykangas L *et al* (2011) A hexanucleotide repeat expansion in C9ORF72 is the cause of chromosome 9p21-linked ALS-FTD. *Neuron* 72: 257–268

Sakai M, Watanabe Y, Someya T, Araki K, Shibuya M, Niizato K, Oshima K, Kunii Y, Yabe H, Matsumoto J *et al* (2015) Assessment of copy number variations in the brain genome of schizophrenia patients. *Mol Cytogenet* 8: 46

Sanjana NE, Shalem O, Zhang F (2014) Improved vectors and genome-wide libraries for CRISPR screening. *Nat Methods* 11: 783–784

Schormann W, Hariharan S, Andrews DW (2020) A reference library for assigning protein subcellular localizations by image-based machine learning. *J Cell Biol* 219: e201904090

Sellier C, Campanari M-L, Julie Corbier C, Gaucherot A, Kolb-Cheynel I, Oulad-Abdelghani M, Ruffenach F, Page A, Ciura S, Kabashi E *et al* (2016) Loss of C9ORF72 impairs autophagy and synergizes with polyQ Ataxin-2 to induce motor neuron dysfunction and cell death. *EMBO J* 35: 1276–1297

Seol JH, Shevchenko A, Shevchenko A, Deshaies RJ (2001) Skp1 forms multiple protein complexes, including RAVE, a regulator of V-ATPase assembly. *Nat Cell Biol* 3: 384–391

Shalem O, Sanjana NE, Hartenian E, Shi XI, Scott DA, Mikkelsen TS, Heckl D, Ebert BL, Root DE, Doench JG *et al* (2014) Genome-scale CRISPR-Cas9 knockout screening in human cells. *Science* 343: 84–87

Shi KY, Mori E, Nizami ZF, Lin Y, Kato M, Xiang S, Wu LC, Ding M (2017) Toxic PRn poly-dipeptides encoded by the C9orf72 repeat expansion block nuclear import and export. *Proc Natl Acad Sci USA* 114: E1111–E1117

Shi Y, Lin S, Staats KA, Li Y, Chang W-H, Hung S-T, Hendricks E, Linares GR, Wang Y, Son EY *et al* (2018) Haploinsufficiency leads to

neurodegeneration in C9ORF72 ALS/FTD human induced motor neurons. *Nat Med* 24: 313

Shu W, Zhao M, Klionsky DJ, Du H (2020) Old factors, new players: transcriptional regulation of autophagy. *Autophagy* 16: 956–958

Sivadasan R, Hornburg D, Drepper C, Frank N, Jablonka S, Hansel A, Lojewski X, Sterneckert J, Hermann A, Shaw PJ *et al* (2016) C9ORF72 interaction with cofilin modulates actin dynamics in motor neurons. *Nat Neurosci* 19: 1610–1618

Soyombo AA, Tjon-Kon-Sang S, Rbaibi Y, Bashllari E, Bisceglia J, Muallem S, Kiselyov K (2006) TRP-ML1 regulates lysosomal pH and acidic lysosomal lipid hydrolytic activity*. *J Biol Chem* 281: 7294–7301

Stoka V, Turk V, Turk B (2016) Lysosomal cathepsins and their regulation in aging and neurodegeneration. *Ageing Res Rev* 32: 22–37

Sullivan PM, Zhou X, Robins AM, Paushter DH, Kim D, Smolka MB, Hu F (2016) The ALS/FTLD associated protein C9orf72 associates with SMCR8 and WDR41 to regulate the autophagy-lysosome pathway. *Acta Neuropathol Commun* 4: 51

Tabke K, Albertmelcher A, Vitavska O, Huss M, Schmitz H-P, Wieczorek H (2014) Reversible disassembly of the yeast V-ATPase revisited under in vivo conditions. *Biochem J* 462: 185–197

Ugolino J, Ji YJ, Conchina K, Chu J, Nirujogi RS, Pandey A, Brady NR, Hamacher-brady A, Wang J (2016) Loss of C9orf72 enhances autophagic activity via deregulated mTOR and TFEB signaling. *PLoS Genet* 12: e1006443

Venkatachalam K, Long AA, Elsaesser R, Nikolaeva D, Broadie K, Montell C (2008) Motor deficit in a *Drosophila* model of mucolipidosis type IV due to defective clearance of apoptotic cells. *Cell* 135: 838–851

Waite AJ, Bäumer D, East S, Neal J, Morris HR, Ansorge O, Blake DJ (2014) Reduced C9orf72 protein levels in frontal cortex of amyotrophic lateral sclerosis and frontotemporal degeneration brain with the C9ORF72 hexanucleotide repeat expansion. *Neurobiol Aging* 35: 1779.e5–1779.e13

Wang C, Telpoukhovskaia MA, Bahr BA, Chen X, Gan L (2018) Endo-lysosomal dysfunction: a converging mechanism in neurodegenerative diseases. *Curr Opin Neurobiol* 48: 52–58

Wang M, Wang H, Tao Z, Xia Q, Hao Z, Prehn JHM, Zhen X, Wang G, Ying Z (2020) C9orf72 associates with inactive Rag GTPases and regulates mTORC1-mediated autophagosomal and lysosomal biogenesis. *Aging Cell* 19: e13126

Wang T, Liu H, Itoh K, Oh S, Zhao L, Murata D, Sesaki H, Hartung T, Na CH, Wang J (2021) C9orf72 regulates energy homeostasis by stabilizing mitochondrial complex I assembly. *Cell Metab* 33: 531–546.e9

Weber RA, Yen FS, Nicholson SPV, Alwaseem H, Bayraktar EC, Alam M, Timson RC, La K, Abu-Remaileh M, Molina H *et al* (2020) Maintaining iron

homeostasis is the key role of lysosomal acidity for cell proliferation. *Mol Cell* 77: 645–655

Wen X, Tan W, Westergard T, Krishnamurthy K, Markandaiah SS, Shi Y, Lin S, Shneider NA, Monaghan J, Pandey UB *et al* (2014) Antisense proline-arginine RAN dipeptides linked to C9ORF72-ALS/FTD form toxic nuclear aggregates that initiate in vitro and in vivo neuronal death. *Neuron* 84: 1213–1225

Xu T, Forgac M (2001) Microtubules are involved in glucose-dependent dissociation of the yeast vacuolar [H+]-ATPase in vivo. *J Biol Chem* 276: 24855–24861

Xu Z, Schaedel L, Portran D, Aguilar A, Gaillard J, Marinkovich MP, Théry M, Nachury MV (2017) Microtubules acquire resistance from mechanical breakage through intralumenal acetylation. *Science* 356: 328–332

Yagi M, Toshima T, Amamoto R, Do Y, Hirai H, Setoyama D, Kang D, Uchiumi T (2021) Mitochondrial translation deficiency impairs NAD+ -mediated lysosomal acidification. *EMBO J* 40: e105268

Yamamoto A, Tagawa Y, Yoshimori T, Moriyama Y, Masaki R, Tashiro Y (1998) Bafilomycin A1 prevents maturation of autophagic vacuoles by inhibiting fusion between autophagosomes and lysosomes in rat hepatoma cell line, H-4-II-E cells. *Cell Struct Funct* 23: 33–42

Yamamoto A, Yue Z (2014) Autophagy and its normal and pathogenic states in the brain. *Annu Rev Neurosci* 37: 55–78

Yambire KF, Rostosky C, Watanabe T, Pacheu-Grau D, Torres-Odio S, Sanchez-Guerrero A, Senderovich O, Meyron-Holtz EG, Milosevic I, Frahm J *et al* (2019) Impaired lysosomal acidification triggers iron deficiency, necrotic cell death and inflammation in vivo. *Elife* 8: e51031

Yang M, Liang C, Swaminathan K, Herrlinger S, Lai F, Shiekhattar R, Chen J-F (2016) A C9ORF72/SMCR8-containing complex regulates ULK1 and plays a dual role in autophagy. *Sci Adv* 2: e1601167

Yang Z, Klionsky DJ (2010) Eaten alive: a history of macroautophagy. *Nat Cell Biol* 12: 814–822

Yu L, Chen Y, Tooze SA (2018) Autophagy pathway: cellular and molecular mechanisms. *Autophagy* 14: 207–215

Zhang C, Lu W, Wang Z, Ni J, Zhang J, Tang W, Fang Y (2016) A comprehensive analysis of NDST3 for schizophrenia and bipolar disorder in Han Chinese. *Transl Psychiatry* 6: e701